MASTER

Measurement of absolute atomic oxygen densities in atmospheric pressure plasma jets

van Grootel, S.C.

Award date:
2013

Eindhoven University of Technology
Department of Applied Physics
Elementary Processes in Gas Discharges (EPG)

Master's Thesis

Measurement of absolute atomic oxygen densities in atmospheric pressure plasma jets

S.C. van Grootel

April 2013 EPG 13-04

Supervisors:
ir. A.F.H. van Gessel
dr. ir. P.J. Bruggeman

Abstract

Atmospheric pressure plasma jets (APPJs) are non-equilibrium plasmas with high reactive species densities at low gas temperature. These plasmas have drawn considerable attention due to their potential for heat sensitive applications such as material functionalization and biomedical applications. Reactive species such as NO, O_3 and O are suggested to play a major role in wound treatment, germ reduction and material functional. To better understand the complicated plasma induced chemistry, detailed analysis of the reactive components in the effluent of the APPJ is required. This work focuses on the analysis of the atomic oxygen density in APPJs.

The absolute atomic oxygen density in atmospheric pressure plasma jets operated with mixtures of He-air or Ar-air is investigated by two-photon absorption laser induced fluorescence (TALIF). TALIF allows to measure in situ the O density, both time and spatially resolved. To obtain absolute densities the fluorescence signal has to be calibrated. For this a known density of xenon atoms is used, which have a two-photon resonance spectrally close to the oxygen transition investigated. Collisional quenching of the fluorescence signal makes it difficult to perform the Xe calibration measurement at atmospheric pressure. TALIF measurements to determine the quenching rates of predefined Xe mixtures were performed in order to develop a calibration method which can be applied at atmospheric pressure. The atomic oxygen TALIF measurements have been performed spatially resolved for different operating powers and air admixtures of the APPJ, and a comparison is made of the O production of a microwave jet with He-air, with gas temperatures of 700-1700K, and a RF jet with Ar-air, with gas temperatures of 400-700K.

Absolute calibrated atomic oxygen densities of microwave plasmas and rf-plasmas have been obtained using a calibration method which makes it possible to do the xenon calibration at atmospheric pressure. For the microwave jet, densities of $3.1{\cdot}10^{22}\mathrm{m}^{-3}$ were found in the core of the plasma, close to the pin electrode. The reproducibility of the measurements is within 20%, the accuracy of the calibrated O density is however 60%. High atomic oxygen densities at positions where the electron density is high suggests that the dissociation of O_2 by free electrons or short lived or metastable species has an important contribution to the production of atomic oxygen in atmospheric pressure plasmas.

Contents

Chapter 1

Introduction

Cold atmospheric pressure plasma jets (APPJs) are a source of non-equilibrium atmospheric pressure plasmas with high reactive species densities at low gas temperature. These plasmas have drawn considerable attention due to their potential for material functionalization and biomedical applications. High concentrations of radicals, suitable for many applications can be provided without the requirement of complicated and expensive vacuum systems. The low gas temperature makes it possible to treat heat sensitive surfaces like living tissue. Possible biomedical applications are wound and antimicrobial treatment and dental applications, and it promises an efficient and improved treatment of infected or chronic wounds [1]. The bacteria killing characteristic of the cold atmospheric pressure plasma is based on direct interaction of the plasma with micro organisms. Just UV radiation or heat results in lower reduction rates, which indicates that the interaction of the chemically active molecules and radicals in the plasma with the bacteria contributes to the bacteria killing [2].

Atomic oxygen (O) is one of the radicals produced in the plasma jet. O is a highly reactive element that readily forms compounds with most elements except the noble gases. Reactive species such as atomic oxygen are supposed to be of major importance regarding wound treatment and germ reduction [3].

Chemical reactions with atomic oxygen in the plasma contribute to the production of nitric oxide (NO) and ozone (O_3). NO, O_3 and O in atmospheric plasmas have been suggested as important species in biomedical plasma applications [4], [5]. For a thorough analysis of the interaction of cold atmospheric pressure plasmas with biomedical materials, a detailed analysis of the reactive components in the effluent of the APPJ is required.

The O density in the plasma can be investigated by optical emission spectroscopy (OES). In OES, the spectrum of the radiation emitted by the plasma is observed and its intensity measured as function of the wavelength. These spectra allow conclusions on the type and number of the excited particles in the plasma and the rotation and vibration temperatures. In case of non-equilibrium plasmas the so-called excitation temperature can be derived. OES only allows to identify excited state species present in the plasma. If absolute calibrated the absolute excited state density could be measured (this is not the ground state density which is much larger). A different method is mass spectrometry, which measures positive and negative ions according to their mass to charge ratio and energy. A disadvantage is that neutral particles have to be ionized before they can be measured. Atomic oxygen ions can be produced from O, but also O_2, which makes it necessary to know the appearance potential. The main issues in MS for plasma diagnostics are however the proper relative and absolute calibration of the MS signal including the

correction of the background signal, and the correct interpretation of the measured data [6]. An alternative method is two-photon absorption laser induced fluorescence (TALIF). TALIF is an optical diagnostic method in which a molecule or atom is excited by a tunable laser. After some time the molecule de-excites and emits a photon. This fluorescence is detected in a TALIF measurement. TALIF has the advantage over OES that the ground state is probed directly. Moreover it is possible to measure absolute densities by performing a calibration measurement, while with OES only relative densities can be measured.

Recently research about NO in APPJs was performed, presenting absolute density distributions of NO and temperature distributions in the APPJ [4], [7]. For O absolute densities are know for APPJ plasmas operated in controlled environments, and for which the measurements for absolute calibration were performed at low pressure (<10 mbar) [8]. The use of a controlled environment significantly change the chemistry in the effluent of the jet, compared to operation in an open environment [1]. Only recent research presented atomic oxygen densities for a APPJ operating in ambient environment, with the absolute calibration measurements performed at low pressure [1].

Because the applications of APPJ are in ambient environment the analysis should also be performed in open environment. Furthermore, it is much more convenient to have a diagnostic method that calibrates the absolute densities at atmospheric pressure. In this work an experimental analysis of the absolute O density distribution in APPJs is investigated by means of TALIF on O. The absolute calibration of the oxygen TALIF signal will be performed by a comparative TALIF measurement on a known amount of xenon atoms, which has a two-photon resonance spectrally close to the oxygen transition investigated. An additional objective is to investigate the possibility of a calibration method, which can be applied at atmospheric pressure. This research is limited to two APPJs, a microwave (MW) driven plasma jet operating in helium air mixtures and a radio frequency (rf) jet operating in argon-air mixtures.

The structure of this thesis is as follows: Chapter 2 gives an overview of the theoretical background, describing TALIF and the involving processes. Furthermore a detailed description of the calibration method for the absolute oxygen density is given. In chapter 3, the experimental TALIF set-up and its different configurations, such as the microwave jet and rf-jet are described. The results are presented and discussed in chapter 4. Finally an overall conclusion is made in chapter 5.

Chapter 2

Theory and background

This chapter starts with background about atmospheric plasmas and plasma sources, followed by a description of air chemistry in a plasma. After that TALIF and the involving processes are described. The final part of this chapter is devoted to a detailed description of the absolute calibration method for the atomic oxygen density in a plasma.

2.1 Atmospheric plasmas

The atmospheric plasmas described in this thesis are generated by electric fields. The electric fields transmits energy to the free electrons. The electronic energy is then transmitted to the neutral species by collisions. The collisions can be elastic or inelastic [9].

- Elastic collisions do not change the internal energy of the neutral species but slightly raise their kinetic energy and thus induce gas heating;
- Inelastic collisions modify, when the energy of the electron is high enough, the electronic structure of the neutral species. It results in the creation of excited species, dissociation of molecules and even ionization. Thus is the source of the chemical reactivity and the charged species in these plasmas.

Two main categories for atmospheric pressure plasma can be distinguished:

- Thermal plasmas have a heavy particle temperature in the order of 10.000 K and a high electron density of the order 10^{21} - $10^{26}\mathrm{m}^{-3}$ [9]. Inelastic collisions between electrons and heavy particles heat the heavy particles, consuming electron energy, which results in an electron temperature of the same order as the heavy particle temperature. The thermal energy is large enough to create reactive species in heavy particle collisions.
- Non-thermal plasmas (equilibrium) have a heavy particle temperature of 300 - 3000K and a lower time averaged electron density of $< 10^{19}\mathrm{m}^{-3}$ [9]. Heavy particles are less efficiently heated by elastic electron collisions, keeping the electron energy high and the electron temperature of the order of 10,000 - 100,000K [9]. Inelastic collisions between electron and heavy particles induce the plasma chemistry.

The two plasma jets investigated in this thesis belong to the category of non-thermal plasmas.

2.2 Plasma jets

There are various types of atmospheric plasma sources, which can be classified by the excitation frequency. The excitation frequency is important since it influences the behavior of the electrons and ions in the plasma. There are the DC, low frequency AC discharges, the RF discharges and the microwave discharges. The discharges can be either in continuous or pulsed mode.

An example of the DC continuous mode is the arc plasma torch, where the pin electrode functions as cathode and the nozzle as anode. The arc is ignited between the cathode and the anode, ionizing the gas flowing through the nozzle.
The (nanosecond) pulsed DC mode enables the injection of large energy amounts in the discharge while limiting the temperature increase of the system. Examples are the corona discharge, where a cathode wire is placed above an anode surface. This results in a moving ionization front towards the surface (streamers). The duration of the pulses is shorter than the time necessary to form an arc. A second example is the low frequency AC discharges which are often dielectric barrier discharges DBD devices, consisting of two plane parallel metal electrodes, or have a coaxial geometry, with at least one covered by a dielectric layer. The gap between the electrode is only a few millimeters to ensure stable operation. Gas flows in the gap. When ignited a multitude of random filaments form between the two electrodes ionizing the gas, which are quenched by charge accumulation on the surface. The barrier limits the current and reduces the lifetime of the plasma filaments which allows to operate it close to room temperature.

In the rf-discharge the electrons are the only ones to follow the oscillations of the electric field. The ions are influenced by the average temporal local values of the field. The rf-plasma jet investigated in this work, consists of two concentric electrodes through which a gas flows. The rf power applied to the inner electrode ionizes the gas, which flows out through the nozzle. A low power enables a stable discharge and avoids an arc transition.

In the microwave discharge the behavior of the electrons and ions are similar as the frequency becomes also large for the e^-. The MW-plasma jet in this work produces a plasma close to an electrode (antenna). Typically MW-plasmas operate at higher gas temperatures compared to rf-discharges at atmospheric pressure.

Atmospheric pressure plasma sources are widely used for materials processing [8]. Sources like arcs and plasma torches provide thermal plasmas with high temperatures. Corona discharges and dielectric barrier discharges generate non-equilibrium plasmas with a low degree of ionization at intermediate gas temperatures. The atmospheric pressure plasma jet can have high reactive species densities at low gas temperatures, making it fit for the use on heat sensitive surfaces.

2.3 Plasma chemistry

The high reactive species densities in APPJs result in a complex system of chemical reactions in which atomic oxygen has an important role. Figure 2.1, as presented by Eliasson *et al* [10], presents an example of the chemistry in a DBD filament indicating the complexity of the chemistry and the many species which can be generated in an atmospheric pressure plasma in air. The reactive particles which are of great importance for biomedical applications are NO, O_3, and O.

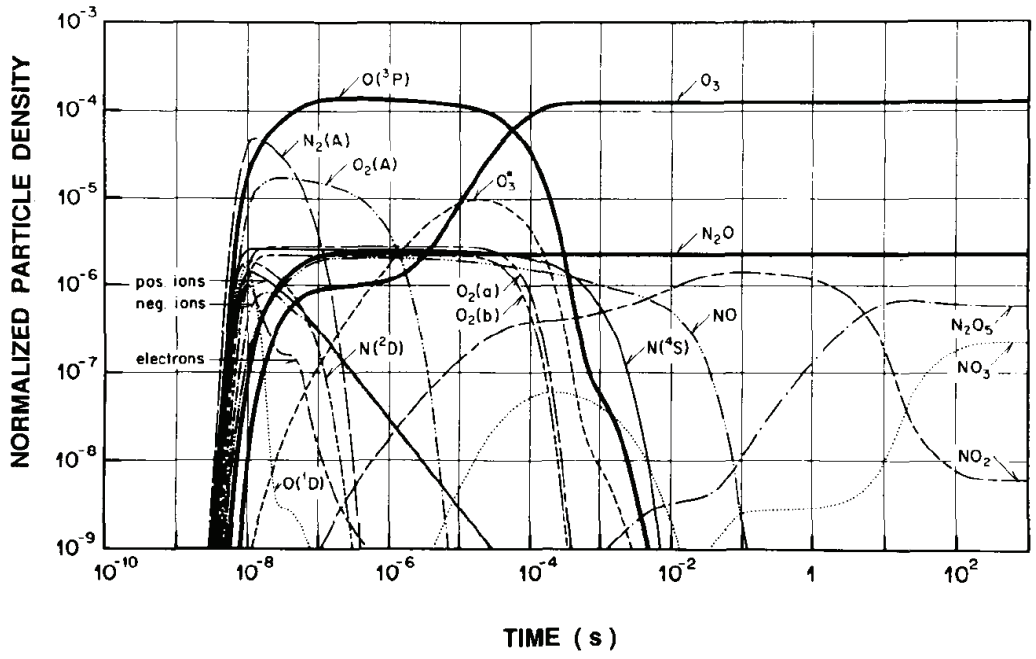

Figure 2.1: Chemical species generated by a microdischarge in "air"(80% N_2 + 20% O_2, p=1 bar, T=300K, homogeneous model) [10].

For a pure O_2 based plasma, the most important reaction path leading to ozone formation is [10],

$$O_2 + e \rightarrow 2O + e. \tag{2.3.1}$$

Followed by a three body reaction,

$$O + O_2 + M \rightarrow O_3 + M \tag{2.3.2}$$

where M is a third collision partner (O_2,O_3 or N_2 (in air)). The O_2 dissociation occurs by electron energies of 6-9eV. When the discharge becomes too strong the atomic oxygen concentration reaches a level at which undesired side reaction gain importance [10], such as

$$O + O + M \rightarrow O_2 + M \tag{2.3.3}$$

and

$$O + O_3 \rightarrow 2O_2. \tag{2.3.4}$$

Both reaction cause a decrease in O and O_3 concentration, indicating that there is an optimum discharge strength at which the oxygen and ozone concentrations are the highest. For air based plasmas nitrogen species add to the complexity of the reaction system. In addition to the O_2 dissociation by electrons, the following reactions have to be taken into account for the generation of O atoms:

$$N + O_2 \rightarrow NO + O \tag{2.3.5}$$

$$N + NO \rightarrow N_2 + O \tag{2.3.6}$$

$$N_2 + O_2 \rightarrow N_2O + O \tag{2.3.7}$$

$$N_2(A, B, C) + O_2 \rightarrow N_2(X) + 2O. \tag{2.3.8}$$

Where N_2(A,B,C) are excited N_2 species [11]. N is generated by the dissociation of N_2 by electrons,

$$N_2 + e \rightarrow 2N + e. \tag{2.3.9}$$

For low temperature APPJ plasmas reaction 2.3.5 is the most dominant [4]. Reactions contributing to the recombination of O and the destruction of O_3 as a result of strong discharges are,

$$O + NO + M \rightarrow NO_2 + M \tag{2.3.10}$$

$$O + NO_2 \rightarrow NO + O_2 \tag{2.3.11}$$

$$NO + O_3 \rightarrow NO_2 + O_2 \tag{2.3.12}$$

The presented reactions indicate that atomic oxygen plays an important role in the generation and destruction of the biomedical interesting species NO, O_3 and O and needs to be studied to understand the plasma induced air chemistry in plasma jets.

2.4 Two-photon laser induced fluorescence (TALIF)

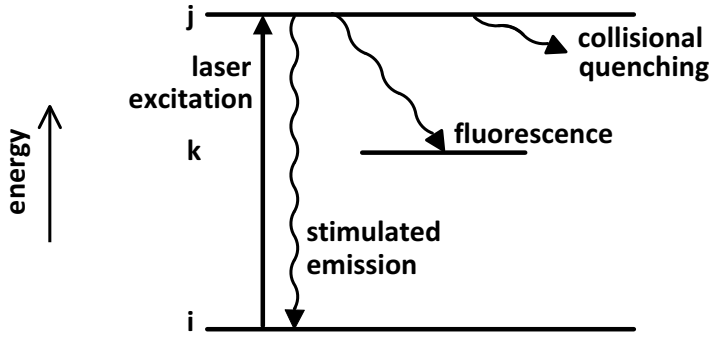

Figure 2.2: Energy diagram for laser induced fluorescence (LIF).

In laser induced fluorescence (LIF) spectroscopy atoms, molecules or ions are irradiated with a laser. When the laser photons have the appropriate wavelength corresponding to a transition of e.g. the molecule, it will excite the ground state to an excited state. Figure 2.2 presents an overview of transitions occurring in a LIF process. Fluorescence refers to the emission of photons by atoms, molecules or ions as a result of absorbing photons. The rate of fluorescence is characterized by the natural lifetime of the excited state (τ_0), which refers to the mean time the e.g. molecule stays in its excited state before emitting a photon. The amount of spontaneous photon emission is influenced by collisional induced quenching, section 2.6.

By varying the laser wavelength over a wide range and measuring the fluorescence photons, an excitation spectrum can be determined. The wavelength of the excitation photon depends on the energy difference of the lower state and excited state level. For some transitions (specifically atomic transitions involving the ground state) the excitation wavelength is located in the vacuum ultra violet (VUV) range. This range, wavelengths shorter than 200 nm, is strongly blocked by air, making it experimentally difficult to perform the measurement in open air. This problem can be avoided by two-photon laser induced fluorescence (TALIF) spectroscopy. By TALIF spectroscopy the excitation is

made by two photons with double the wavelength of the single photon excitation. Figure 2.3 presents the energy diagram for a TALIF process. After absorption of one photon, an intermediate "virtual" energy level is obtained, indicated with a 4 in figure 2.3. If within the lifetime of the energy level a second photon is absorbed, the atom will be excited. The energy and lifetime of the "virtual" level uphold the uncertainty principle,

$$\Delta E \Delta t \geq \frac{\hbar}{2} \tag{2.4.1}$$

meaning that the energy and lifetime of the "virtual" state can not both be defined accurately and the laser wavelength does not need to match exactly an energy level of an excited state.

A disadvantage of two-photon excitation is that it is considerably less efficient than single photon excitation. The fluorescence intensity scales linearly with the square of the laser intensity [12]. This means that in most cases the laser energy has to be increased to obtain a fluorescence signal, which can be done by focusing the laser beam. Focusing the laser beam entails increased spatial resolution. However focusing the laser also increases the possibility of resonantly enhanced multi-photo-ionization (REMPI) and amplified stimulated emission (ASE), which reduce the fluorescence signal and causes the signal intensity to deviate from the quadratic dependence on the laser intensity. In TALIF measurements it is a requirement that the observed fluorescence wavelength differs from the laser wavelength. It is a requirement because emitted photons with a wavelength equal to the laser wavelength could be reabsorbed by the ground state atoms, causing the fluorescence intensity to deviate from the quadratic dependence on the laser intensity. Furthermore, it is more difficult to measure, the detector needs to make a difference between the light source and the fluorescence.

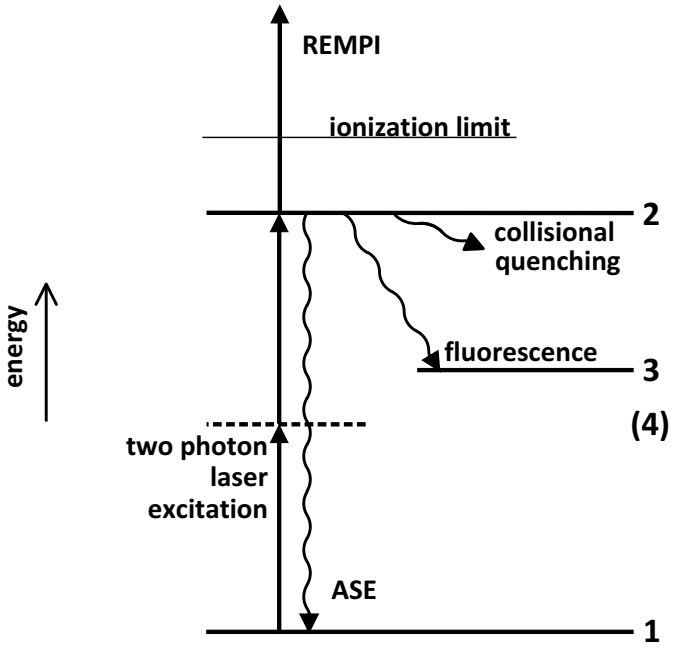

Figure 2.3: Energy diagrams for two-photon absorption laser diagnostics. Showing the possible transitions occurring during a TALIF process.

2.5 TALIF on O and Xe

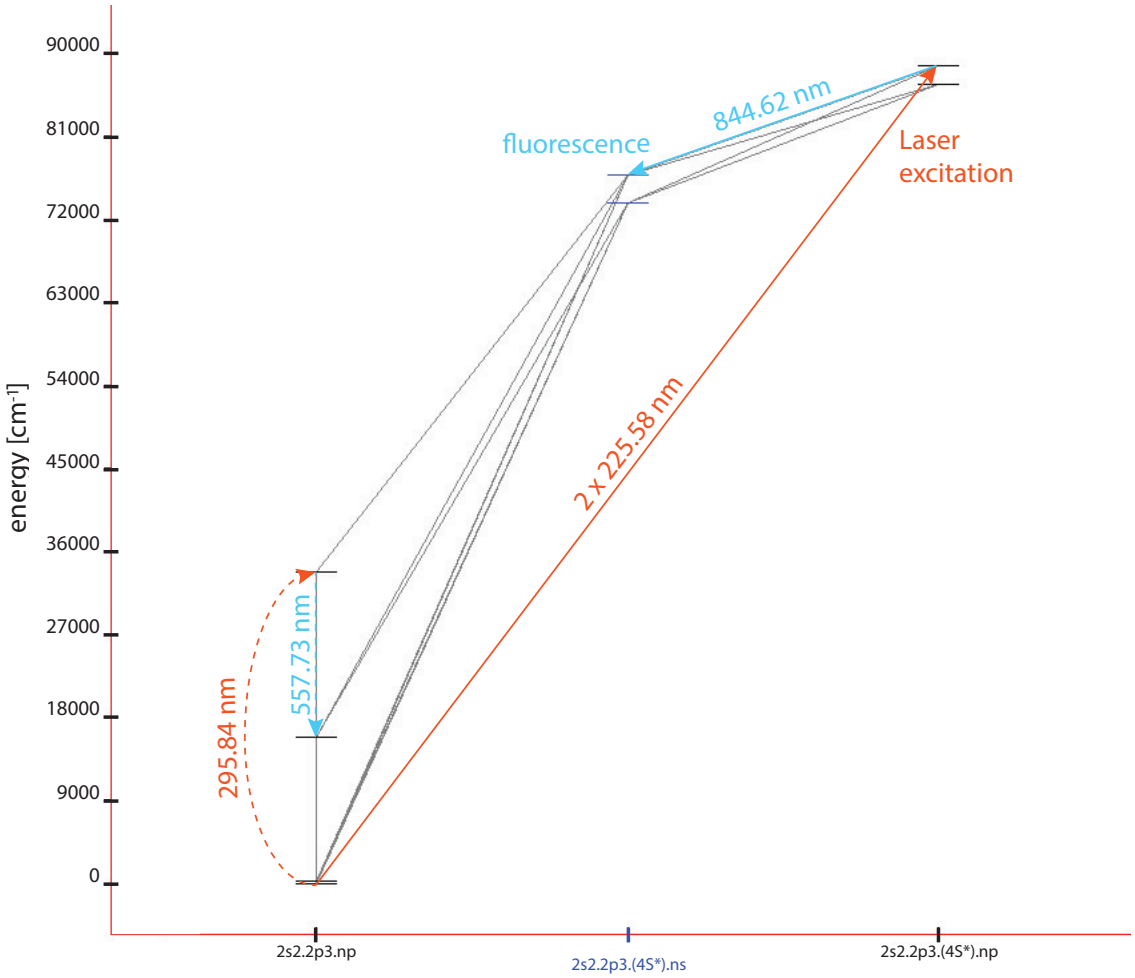

Figure 2.4: Grotrian diagram of O(I) [13]. The excitation process to determine the atomic oxygen density used in the TALIF measurement is indicated with solid arrows. A possible LIF transition is indicated with dotted arrows.

Figure 2.4 presents the Grotrian diagram for atomic oxygen with an indication of the TALIF process. The figure also indicates a possible LIF transition on O, where the ground state level $2p^4\ ^3P_J$ is excited to the $2p^4\ ^1S_0$ level, after which spontaneous emission occurs to the $2p^4\ ^1D_2$ level. However the spontaneous emission coefficient for this transition is very weak (A=1.26s^{-1} compared to A=3.22·10^{7}s^{-1} for the TALIF process [13]), which makes it very difficult to detect, therefore a different transition is needed, which requires TALIF. A schematic overview of the atomic oxygen and xenon transitions, as used for the absolute calibration of atomic oxygen, is presented in figure 2.5. The ground state of atomic oxygen, $2p^4\ ^3P_J$, has three levels with angular momentum quantum number $J = 2, 1, 0$, where the $J = 2$ level has the lowest energy and the $J = 0$ level the highest. The splitting of the ground state (227cm^{-1}) is comparable to the mean kinetic energy at room temperature (k_bT =209cm^{-1} for $T = 300$K). If the ground state exhibits a thermal population distribution, only a TALIF measurement of one ground state sub-level has to be performed in order to determine the total ground state population (see section 2.7).

The excitation wavelength of ground state atomic oxygen to the 3p ^{3}P$_J$ level is in

the VUV range, so to perform fluorescence measurements in atmospheric pressure air conditions, TALIF is needed. The excitation of the ground state of atomic oxygen occurs with a laser wavelength of approximately 225.58nm.

The 3p $^3\mathrm{P}_J$ state of atomic oxygen also consists of three levels, with $J = 1, 2, 0$ where the $J = 1$ level has the lowest energy and the $J = 0$ level has the highest energy. The de-excitation of the excited state level occurs by photon emission with a wavelength of approximately 844.62 nm or collisional quenching. The energy levels of the 3p $^3\mathrm{P}_J$ state are so close together, that the line profile of the three de-excitation transitions overlap for typical dye laser line widths used during this research, (see figure 2.5). Figure 2.5 shows that the population of the three excited levels, 3p $^3\mathrm{P}_{1,2,0}$ is different for each excitation of the different ground state levels, $2p^4\ ^3P_{2,1,0}$. An explanation for this occurrence has not been found in literature. However the figure also shows that the peaks for $\Delta J = 0$, are the largest and that only this level and the level direct above or below this level are populated. So only for $J = 2$, which is the middle level, are there three levels populated. From this a possible explanation is that only transitions with $\Delta J = 0$ are allowed, and that the second (and third) peak come from population by e.g. collisional transitions.

The levels involved in the TALIF transitions for xenon are all singlet states, with a laser excitation occurring with a wavelength of 224.24nm and a fluorescence signal with a wavelength of 834.68nm.

It has been observed that the excited state level of xenon 6p $^2[3/2]_2$ quenches strongly to the 6p $[3/2]_2$ level, which has a transition by spontaneous emission to the 6s $[3/2]_2$ level. The emitted photons have a wavelength of 823,16nm. The importance of this will be made clear further-on.

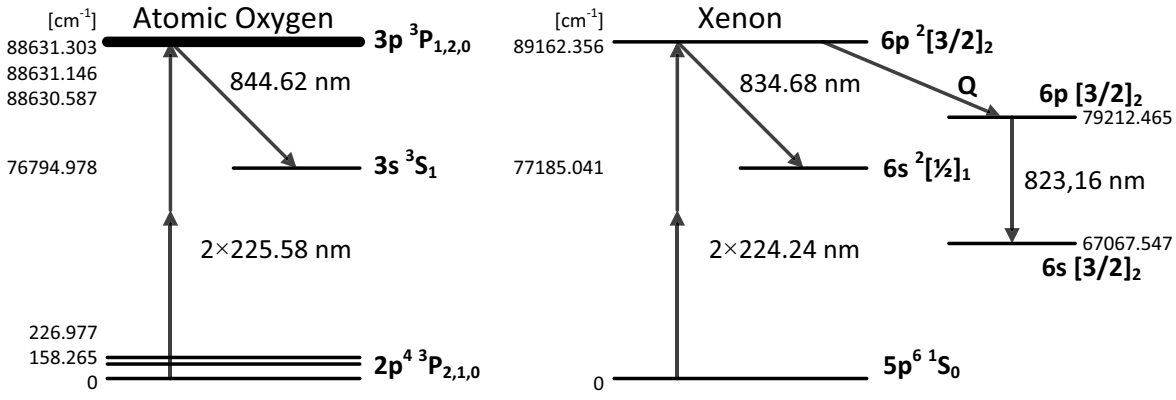

Figure 2.5: Energy levels and TALIF transitions for atomic oxygen and xenon. The Q mentioned in the xenon scheme represents a transition by collisional quenching.

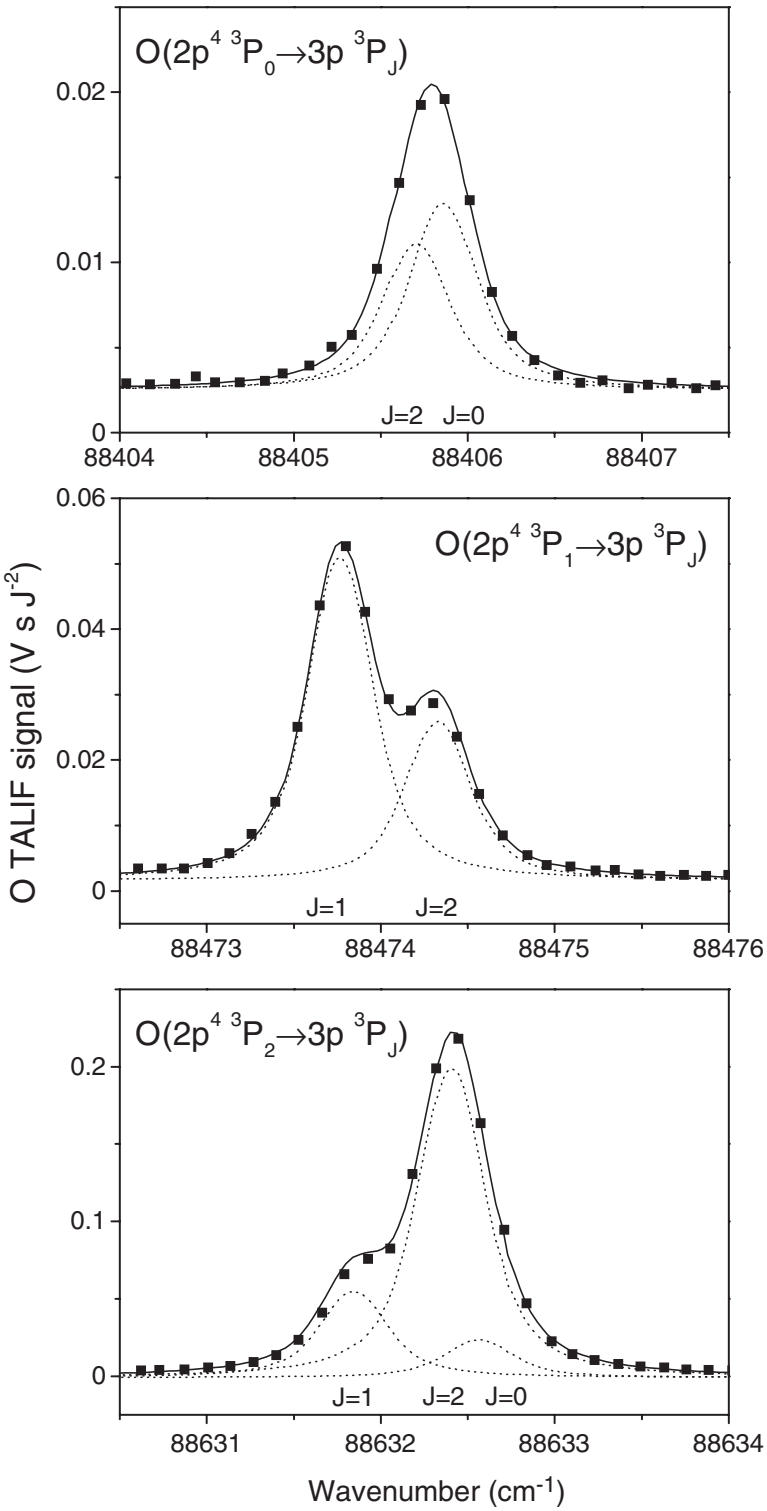

Figure 2.6: Two-photon excitation line profiles of the O($2p^4 {}^3P_{2,1,0} \rightarrow 3p^3 P_{1,2,0}$) fine structure components [8]. The solid curves are fits, consisting of superpositions of Voigt profiles (dotted curves), to the measuring points. Measured for 705 sccm He and 3.5 sccm O_2 fluxes at 985 Pa total pressure and 50W MW power.

2.6 Collisional quenching

There are multiple processes that can de-populate an excited state other than de-excitation by emitting a photon. Examples are de-excitation through collisions with heavy parti-

cles or excitation/ ionization by inelastic electron collisions. These processes reduce the fluorescence radiation during a TALIF measurement and are referred to by collisional induced quenching. Figure 2.3 presents an overview of processes that can occur during TALIF measurements. Collisional quenching is dependent on the pressure, temperature, and the collision partners. A pressure dependence of the effective quenching rate is linear for pressures of a few mbar [14]. At these low pressures, the collisional quenching occurs in two particle reactions for which the effective quenching rate can be expressed as,

$$Q = \sum_q k_q^{(1)} n_q \tag{2.6.1}$$

where $k_q^{(1)}$ and n_q represent the specific quenching coefficient for two particle reactions and the number density of the collision partner q, respectively.

When the pressure increases three particle quenching may start to occur, which adds a quadratic term to the effective quenching rate,

$$Q = \sum_q k_q^{(1)} n_q + k_q^{(2)} n_q^2 \tag{2.6.2}$$

where $k_q^{(2)}$ represent the specific quenching coefficient for three particle reactions. The quenching coefficients can be derived from a so-called Stern-Volmer plot. This plot represents the pressure dependence of the effective de-excitation rate (A). The effective de-excitation rate can be expressed by,

$$A = \frac{1}{\tau_0} + Q = \frac{1}{\tau_0} + \sum_q k_q^{(1)} \frac{p_q}{k_b T} + \sum_q k_q^{(2)} \left(\frac{p_q}{k_b T} \right)^2 \tag{2.6.3}$$

where τ_0 is the natural lifetime, which can be determined by extrapolating the curve to $p = 0$. The pressure dependence of the effective de-excitation rate can be determined by measuring the fluorescence decay time constant at different pressures. The particle quenching coefficients follow from the derivative of the curve in the linear region. At atmospheric pressures equation 2.6.2 applies. In some cases the quenching rate at atmospheric pressure becomes so large, that it is impossible to determine the effective de-excitation rate with a nanosecond pulsed laser measurement (see further).

2.7 Boltzmann distribution

If the ground state of atomic oxygen in the helium-air plasma exhibits a thermal population distribution, the total atomic oxygen population in ground state can be determined from one ground state sub-level with energy E_J, by considering the corresponding Boltzmann population fraction $f_O(T)$, or Boltzmann factor;

$$f_O(T) = \frac{n_J}{\sum_J n_J} = \frac{(2J+1)\exp\left(\frac{-E_J}{k_b T}\right)}{\sum_J (2J+1)\exp\left(\frac{-E_J}{k_b T}\right)}. \tag{2.7.1}$$

Equation 2.7.1 can also be used to determine the gas temperature T of the plasma, by determining the atomic oxygen population in all three sub-levels of the ground state. This can be obtained by expressing the species density in state J as,

$$n_J = C_1(2J+1)\exp\left(\frac{-E_J}{k_b T}\right). \tag{2.7.2}$$

This expresion can be rewritten as,

$$\ln\left(\frac{n_J}{(2J+1)}\right) = \frac{-E_J}{k_b T} + C_2. \tag{2.7.3}$$

It shows that the gas temperature can be derived from the slope of the so called Boltzmann plot,when a log-plot is made from the density reduced by the degeneracy (2J+1) as a function of E_J.

2.8 Principle of TALIF and absolute calibration

For the calibration of the absolute density of the atomic oxygen in a atmospheric pressure plasma by means of a reference measurement with xenon gas of known concentration, an equation has been derived. This section gives a more detailed description of the procedure and derivation as is given in the original paper on which the method used here is based [14]. The derivation describes a general case for which the transitions occur in a three level system as is presented in figure 2.3, where 1 indicates the ground state, 2 the excited state after absorbing two photons and 3 an intermediate state to which de-excitation by means of photon emission takes place.

This simplified model applies to xenon for which the ground state and excited state are singlet states. However, for atomic oxygen the fine structure has to be considered. Although the ground state and excited state are both triplet states, this model can still be applied to determine the total atomic oxygen density in the ground state. Because the excited state sub-levels of atomic oxygen lay close together the signals coming from the de-excitation of the three levels spectrally overlap, so they contribute all to the total signal and therefore the excited state of the model can be simplified to one level. The bandwidth of the laser is small enough to excite the sub-levels of the ground state of atomic oxygen individually, meaning that the total atomic oxygen density must be determined by three individual measurements or by assuming a Boltzmann distribution of the three levels.

The derivation of the calibration equation is given below.

When the laser intensities are sufficiently low, a photo-ionization effects of the excited state population $n_2(t)$ can be neglected. The rate of change of the populations of the first two levels can be expressed by the two-photon excitation rate $R(t)$ and the effective de-excitation rate A_2 [14],

$$R(t) = G^{(2)}\sigma^{(2)}g(\Delta\nu)\left(\frac{I_0(t)}{h\nu}\right)^2 \tag{2.8.1}$$

$$A_2 = \tau^{-1} + Q$$

,as

$$\frac{d}{dt}n_2(t) = R(t)n_1(t) - A_2 n_2(t) \tag{2.8.2a}$$

$$\frac{d}{dt}n_1(t) = -R(t)n_1(t) \tag{2.8.2b}$$

- $G^{(2)}$ is the Photon static factor. It account for statistical fluctuations of the laser intensity and is defined as:
$$G^{(2)} = \frac{\langle I(t)^2 \rangle}{\langle I(t) \rangle^2}$$
- $\sigma^{(2)}$ is the generalized two photon excitation cross section;
- $g(\Delta\nu)$ is the normalized ($\int g(\nu)d\nu = 1$) line profile of the two-photon excitation, which is the convolution of the laser profile $g_L(\nu)$ with the central frequency ν_L and the absorption line shape of the atom $g_A(\nu)$ with as central wavelength the two-photon resonance frequency ν_A according to

$$g(\Delta\nu = 2\nu_L - \nu_A) = g_A(2\nu - \nu_A) * g_L(\nu - \nu_L) * g_L(\nu - \nu_L); \qquad [14]$$

- $I_0(t)$ is the laser intensity in Wcm^{-2};
- $h\nu$ stands for the photon energy of the absorbed photon;
- τ is the natural lifetime of the excited state;
- Q is the effective collisional quenching quenching rate.

In the case of measurements on atomic oxygen, the excitation transitions induced by the laser also occurs due to electron excitation in the plasma, this is the main source of the background radiation. This background radiation is, in the case of the MW plasma, constant in time and therefore it is easy to subtract to only obtain the fluorescence as modeled (see further).

From equation 2.8.2b an expression for n_1 can be derived,

$$n_1(t) = n_0 \exp\left(-\int_0^t R(t')dt'\right). \tag{2.8.3}$$

When the laser intensities are sufficiently low, a depletion of the ground-state population can be neglected, $n_1(t) \approx n_0$ is constant, where $n_0 = n_1(0)$. This leads to a simplification of equation 2.8.2a,

$$\frac{dn_2(t)}{dt} + A_2 n_2(t) = R(t)n_0. \tag{2.8.4}$$

Solving this differential equation and noticing that at $t = 0$ there is no laser excitation,

so $n_2(0) = 0$, leads to,

$$n_2(t) = n_0 \int_0^t R(t')e^{-A_2(t-t')}dt'. \tag{2.8.5}$$

Substituting the two-photon excitation rate $R(t)$, equation 2.8.1, into equation 2.8.5, describes a convolution integral of the functions $y_1 = \alpha I_0^2(t)$ and $y_2 = e^{-A_2 t}$,

$$n_2(t) = (y_1 * y_2)(t) \tag{2.8.6}$$

with,

$$\alpha = n_0 G^{(2)} \frac{\sigma^{(2)}}{(h\nu)^2} g(\Delta\nu).$$

The number of fluorescence photons emitted per unit volume in the fluorescence channel, n_F, can be found by:

$$n_F = A_{23} \int_0^\infty n_2(t)dt. \tag{2.8.7}$$

By using the mathematical property that states that the area under a convolution of two functions is the product of the areas of the two functions [15], equation 2.8.7 can be simplified to,

$$n_F = n_0 a_{23} G^{(2)} \frac{\sigma^{(2)}}{(h\nu)^2} g(\Delta\nu) \int_0^\infty I_0^2(t)dt. \tag{2.8.8}$$

In which $a_{23} = A_{23}/A_2$ is the optical branching ratio. Integration of equation 2.8.7 over the two-photon resonance λ_r and the observed excitation volume V_O, taking the detector sensitivity and collection efficiency into account, results in the time and spectrally integrated photomultiplier signal S_{PMT},

$$S_{PMT} = \frac{\Delta\Omega}{4\pi} T\eta G e_0 R_L \int_{\lambda_r} \int_{V_O} n_F(\vec{r})dV d\nu \tag{2.8.9}$$

- $\Delta\Omega$ stands for the solid angle of detection;
- T is the transmission of the detection optics;
- η is the quantum efficiency of the photomultiplier;
- G is the amplification of the photomultiplier;
- e_0 stands for the elementary charge;
- R_L is the load resistor of the photomultiplier.

A normalized fluorescence signal I_F can be obtained by:

$$I_F = \frac{S_{PMT}}{\int\int I_0^2(t,\vec{r})dtdV}. \tag{2.8.10}$$

By combining equations 2.8.8, 2.8.9 and 2.8.10 the following expression for I_F is obtained,

$$I_F = \frac{\Delta\Omega}{4\pi} T\eta G e_0 R_L n_0 a_{23} G^{(2)} \sigma^{(2)} \frac{\int\int\int_0^\infty \frac{g(\Delta\nu)}{(h\nu)^2} I_0^2(t)dtdVd\nu}{\int\int I_0^2(t,\vec{r})dtdV}. \tag{2.8.11}$$

This equation relates the ground state density to the fluorescence intensity.

Relative densities are easy but for absolute values several unknowns need to be determined (such as angle of detection, quantum efficiency of the photomultiplier, detection volume, etc), see equation 2.8.11. An alternative is to calibrate with xenon gas, which has a known ground state density and an excitation at approximately the same wavelength as O, as was discussed in section 2.5. The expression for the atomic oxygen density can be derived by dividing I_F for xenon by I_F for atomic oxygen. If for both cases, described by figure 2.5, the TALIF excitations are performed with identical spatial, spectral, and temporal intensity distribution of the laser radiation, only the following terms will remain[1]:

$$\frac{I_{F,Xe}}{I_{F,O}} = \frac{n_{Xe}^0}{n_O^0} \frac{a_{Xe}^{23}}{a_O^{23}} \frac{\sigma_{Xe}^{(2)}}{\sigma_O^{(2)}} \left(\frac{h\nu_O}{h\nu_{Xe}}\right)^2.$$

Furthermore, equation 2.8.10 can be expressed as,

$$I_F = \frac{S_{PMT}}{E^2} \tag{2.8.12}$$

where E is the laser energy in Joule. After rearranging the parameters, the equation for calibrating the absolute atomic oxygen density is obtained,

$$n_O = \frac{\sigma_{Xe}^{(2)}}{\sigma_O^{(2)}} \frac{a_{Xe}}{a_O} \frac{I_{F,O}}{I_{F,Xe}} \left(\frac{h\nu_O}{h\nu_{Xe}}\right)^2 n_{Xe}. \tag{2.8.13}$$

[1]The calibration equation derived in [14] includes the ratio of the detection sensitivities for the observed fluorescence wavelengths. Because the two-photon resonances in this project are spectrally closer together than the ones used in [14], $\Delta\lambda$ =10nm compared to $\Delta\lambda$ =380nm, this term can be considered to be one in this work.

Chapter 3

Experimental setup and calibration method

In this chapter the experimental setup is described. First the general TALIF setup followed by the description of two plasma jets and the vacuum system.

3.1 TALIF setup

The experimental setup for the TALIF measurements with the microwave plasma jet is presented in figure 3.1.

The excitation of the ground state atoms (O, Xe) is realized with a Sirah cobra dye laser, which is pumped with a YAG laser at 355 nm. To create the UV necessary for excitation of the ground state atoms the dye laser uses a Coumarin 2 dye and the produced radiation at 442-454nm is frequency doubled by a BBO crystal, resulting in a tunable laser range of about 221-227nm. The bandwidth of the laser light before doubling by the BBO crystal is 1.4 pm, which is reported as a specification of the laser. The laser is pulsed with frequencies of 1000 Hz, 2000Hz or 4000 Hz, depending on the desirable laser energy per pulse, since a lower frequency results in a higher laser energy per laser pulse. The laser beam is focused with a quartz lens with a focal length of 250mm, to increase the laser energy per unit area. The focal point of the lens is located above the center of the jet. The laser energy is measured by an Ophir photo-diode energy sensor. The fluorescence photons are collected perpendicularly to the laser beam by two quartz lenses with focal lengths of 200mm each. The focal point of the first lens collides with the focal point of the focused laser beam. The second lens projects the fluorescence photons on the entrance slit of a Jarrell-Ash 82025 monochromator with 0.5m focal length and a blaze of 300 nm. The monochromator is used to measure the fluorescence signal corresponding to the excitation of one ground state level. The wavelength setting of the monochromator is set so that the signal is at its maximum. A photomultiplier (Hamamatsu R666) is connected to the exit of the monochromator. The photomultiplier operates in photon counting mode. The pulses from the photomultiplier are amplified and counted by a computer with a Fast Comtec P7888 time digitizer. The time resolution of the time digitizer is 1ns. A photo of the experimental setup concerning the detection of the fluorescence signal is presented in figure 3.2.

A measurement is performed by scanning the dye laser with constant velocity over the wavelength range of the fluorescence spectrum. For each step in wavelength a time resolved histogram of counts is accumulated over a set number of laser shots. This way

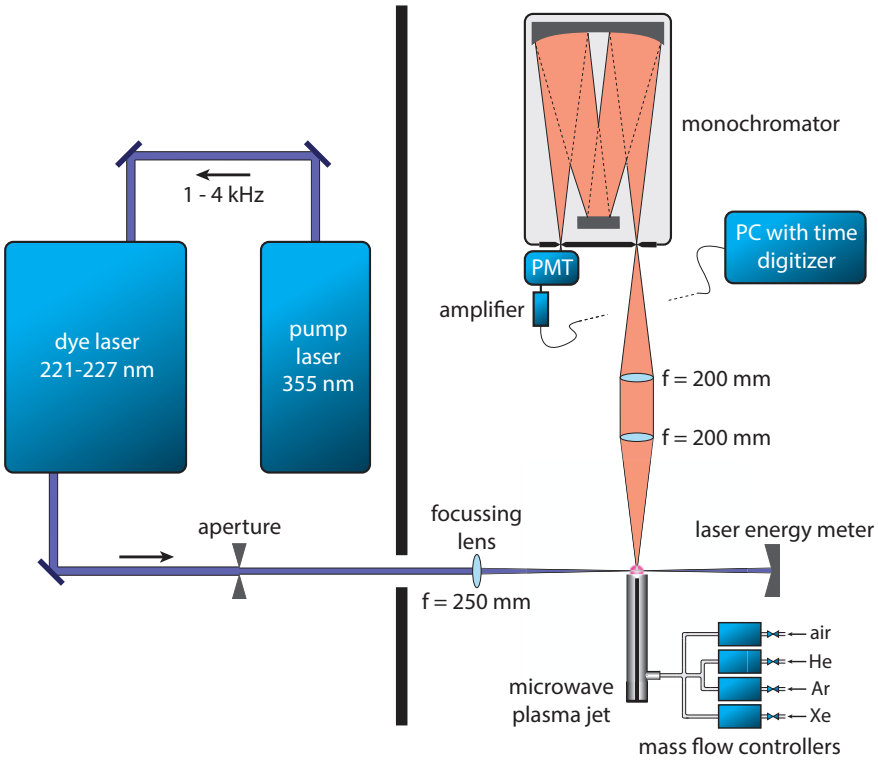

Figure 3.1: Experimental setup for the TALIF measurements, with the microwave jet as plasma source.

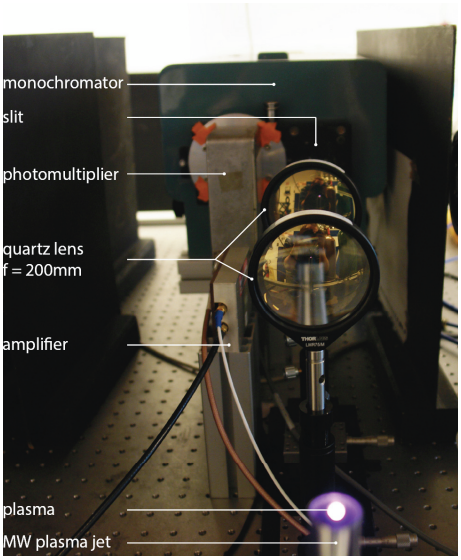

Figure 3.2: Photo of the detection part of the experimental setup for TALIF measurements with the microwave jet as plasma source, concerning detection of the fluorescence signal.

it is possible to measure both time resolved and wavelength resolved at the same time. A result of a TALIF measurement is presented in figure 3.3; On the horizontal axis the wavelength of the laser is plotted, the measured time per pulse is plotted on the vertical axis, and the TALIF intensity is given in counts. The number of counts is dependent on the number of shots per step in wavelength.

The number of laser shots per point, the measurement duration, and the scan range of the laser wavelength can be set manually. Because the velocity of the scan is constant, the accuracy of a measurement can by increased by increasing the measurement duration and/or the amount of shots per point.

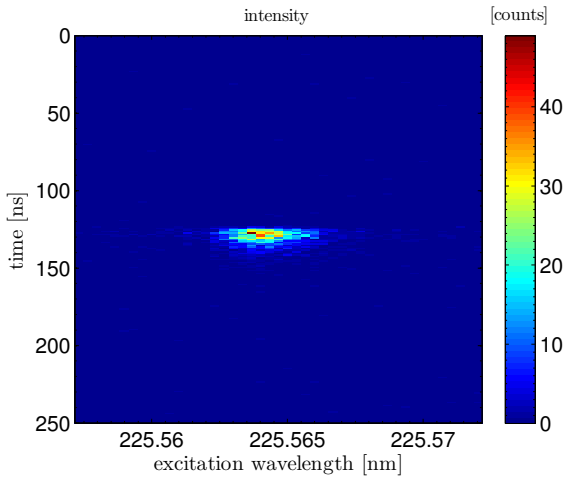

Figure 3.3: Time and wavelength resolved atomic oxygen TALIF signal for a MW plasma with a gas flow of 6slm helium with 3.2% air. The ground state $J = 2$ was used for a measurement with a duration of 90s, a laser frequency of 2000Hz, 4000 shots per point, and scanned over a wavelength range of 225.560 - 225.575nm.

For each step in wavelength the TALIF signal is corrected for background, which is determined by taking the mean of the signal over the time range where there is no TALIF signal. By integrating the background corrected measurement result over time, a wavelength resolved TALIF signal or spectrum can be obtained. Integrating over the wavelength gives the time resolved TALIF signal. Figure 3.4 presents the wavelength resolved TALIF signal and the time resolved TALIF signal obtained from figure 3.3. The time resolved signal can be used to determine the effective de-excitation rate of the TALIF intensity, by fitting a convolution of the square of the laser profile and an exponential curve, equation 2.8.6, through the data points. The laser profile was determined by Rayleigh scattering. Figure 3.5 (left) shows the laser profile, figure 3.5 (right) presents a fit with a time constant τ of 4.5ns, which yields a de-excitation rate of $A_2 = 2.2 \cdot 10^8 \mathrm{s}^{-1}$.

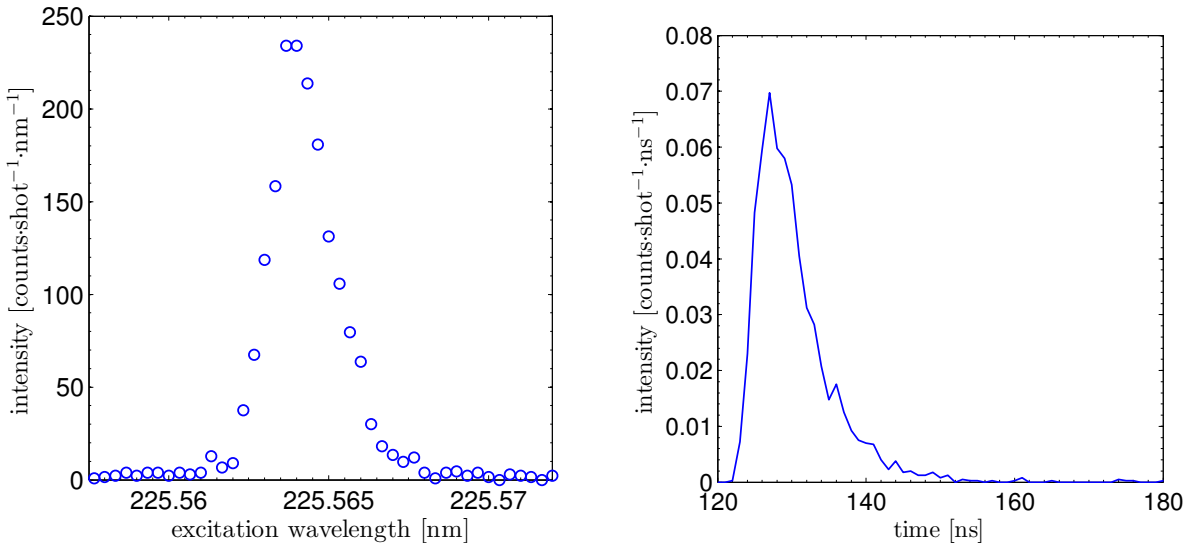

Figure 3.4: Time integrated TALIF signal (left) and the wavelength integrated TALIF signal (right) obtained from the measurement results presented in figure 3.3.

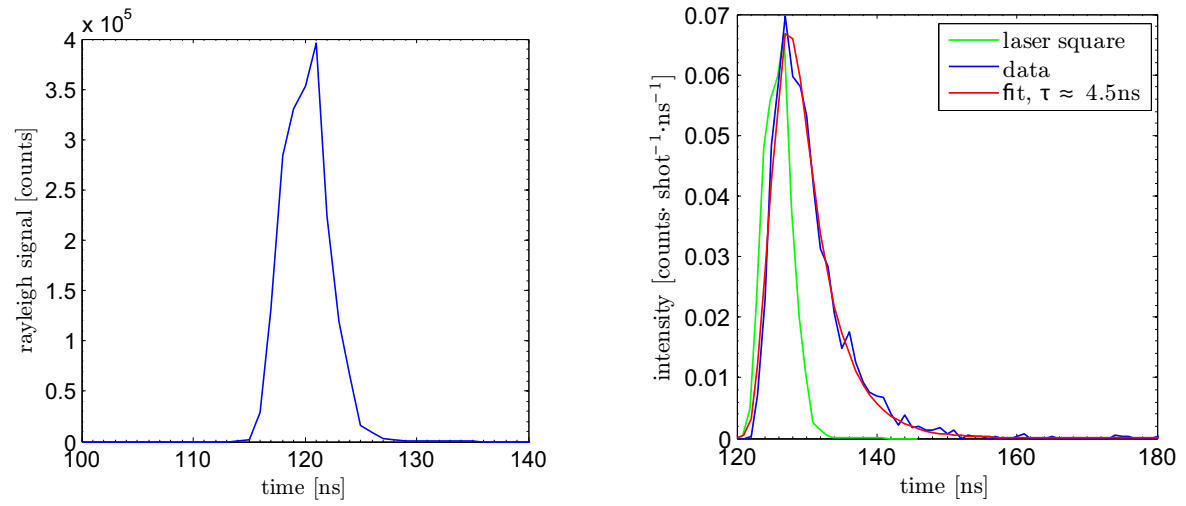

Figure 3.5: Left: Laser profile measured with Rayleigh scattering on argon with a laser wavelength of 226nm. Fit of a wavelength integrated TALIF signal using the convolution of the laser profile squared and an exponential function.

3.2 Microwave plasma jet

An overview of the microwave plasma jet setup is presented in figure 3.6. The microwave plasma jet (see also Hrycak *et al* [16]) consist of a metal tube with an inner diameter of 12 mm and in the center a pin electrode connected with coaxial cables and a circulator to a Microtron 200 microwave power generator (2.45GHz). The outer tube electrode is grounded. The microwave jet operates in open air and was mounted on a motorized stage, which can move in the plane perpendicular to the laser beam. At the zero position, both radial and axial position are zero, the laser is focused above the center of the jet and passes the top of the jet as close as possible, without decreasing the measured laser energy.

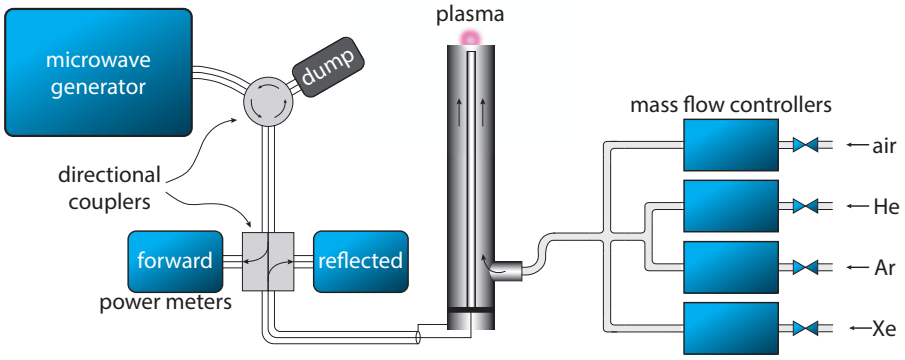

Figure 3.6: Experimental setup for the microwave jet.

In case of a plasma, a gas flow of 6slm He plus 0 - 0.4slm (0 - 6%) dry air was flowing through the tube with a flow speed of 0.9ms^{-1}. The plasma power was determined by subtracting the reflected microwave power from the forward microwave power. The forward and reflected microwave powers were measured with two thermal head detectors connected to a directional coupler. The plasma power was varied between 20-56W. Measurements were performed at radial positions ranging from -4mm up to +4mm and axial positions ranging from 0.1mm up to 16mm.

The microwave plasma looks like a small ball located on the top of the pin electrode, as is shown in figure 3.7. The gas temperature in the center of the plasma is typically between 1200K and 1800K [4].

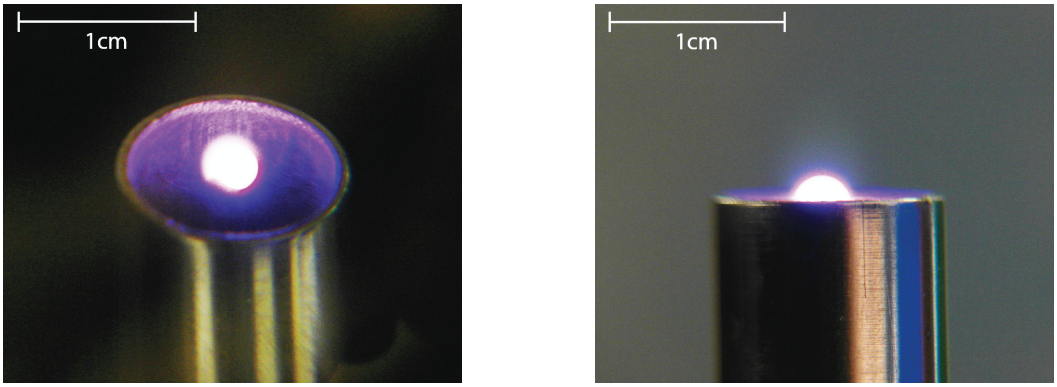

Figure 3.7: Photos of a 30W microwave plasma, with a gas flow of 6slm He plus 3.2% air. Left: A view of the whole plasma. Right: A sideview of the jet, from which can be derived that at the zero position the laser goes through the center of the plasma.

For the calibration measurements with xenon the microwave generator was turned off, so that the jet only functioned as a gas outlet. The xenon measurements, needed to calibrate the atomic oxygen density for the O measurements performed on both the MW-jet and the RF-jet, were performed with the tube of the MW-jet. For the calibration measurements for the MW-jet a gas flow of 2.5slm argon plus 0.2% xenon was flowing through the tube, with a flow speed of 0.4ms^{-1}. For the calibration measurements for the rf-jet a gas flow of 5slm argon plus 0.2% xenon was flowing through the tube, with a flow speed of 0.7ms^{-1}. All xenon measurements were performed at a radial position of 0mm and an axial position of 0.5mm.

3.3 RF-plasma jet

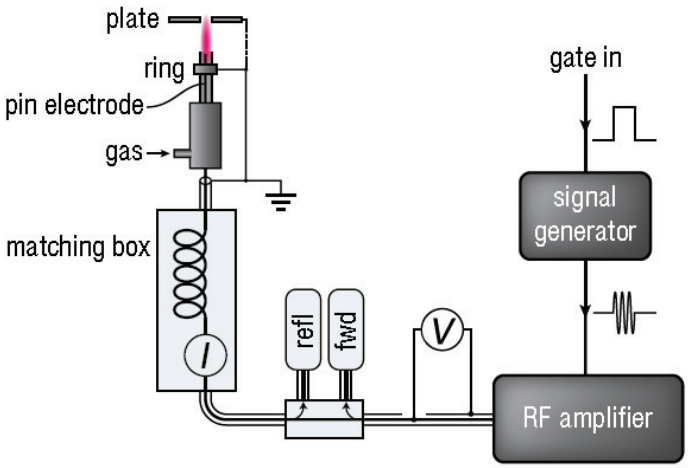

Figure 3.8: Experimental setup of the rf-jet [7].

The rf-plasma jet is like the microwave jet an atmospheric pressure plasma jet, which operates in open air. However, while the microwave jet operates in continues mode, the rf-jet is time modulated. By operating the rf-jet in pulsed mode, lower gas temperatures are obtained, which are more suitable for e.g. wound treatments.

The rf-jet consists of a glass tube with an inner diameter of 1.7mm attached to a plastic holder. The glass tube contains a needle electrode with at diameter of 1mm, which is connected to an E&I A075 RF amplifier driven at 13.9MHz via a homemade matching box. The matching box consisting of a coil and matches the impedance of the plasma with the power supply. Figure 3.8 presents an overview of the rf-jet setup. Two types of grounded electrodes were used for two different configurations, a ring or a plate. The ring is placed around the glass tube, while the plate, with a thickness of 0.5mm and an opening of 5.0mm in the middle, is mounted above the glass tube. In figure 3.9 a schematic of the top of the rf-jet is presented with both the ring electrode configuration and the plate electrode configuration.

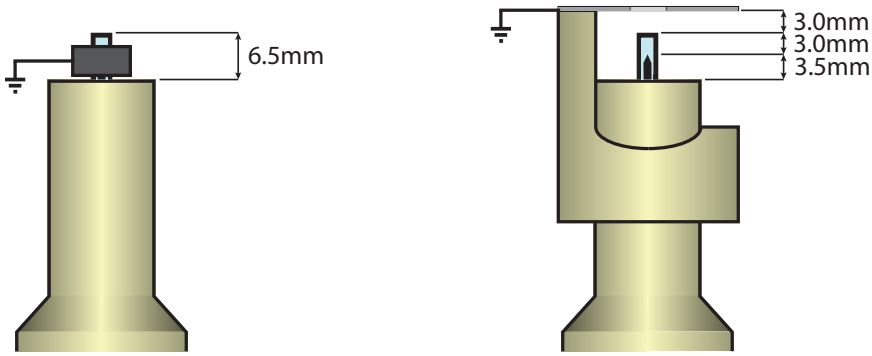

Figure 3.9: Schematic of the top of the rf-jet with left the ring electrode configuration and right the plate electrode configuration. The needle is the rf driven electrode.

A gas flow of 1slm Ar with a varying amount of 0 - 42sccm (0 - 4%) of either dry air,

oxygen or nitrogen was flown through the glass tube. The 13.9MHz at which the plasma is operated is generated by a HP 8116A signal generator and time modulated at 20kHz with 20% duty cycle by a BNC 575 pulse/delay generator. This time modulated signal is amplified by the E&I RF amplifier. A representation of the operating signal is presented in figure 3.10.

The power dissipated by the plasma was determined from measurements of the forward and reflected RF power coming from and going to the amplifier. These powers were measured by using an Amplifier Research PM2002 with PH2000 dual diode power heads connected to a directional coupler. Like the microwave jet, the rf-jet is mounted on a motorized stage so that the rf-jet can be positioned in both radial and axial direction with an accuracy of 10μm. In the zero position the laser is focused above the center of the glass tube and passes the top as close as possible, without decreasing the laser energy measured.

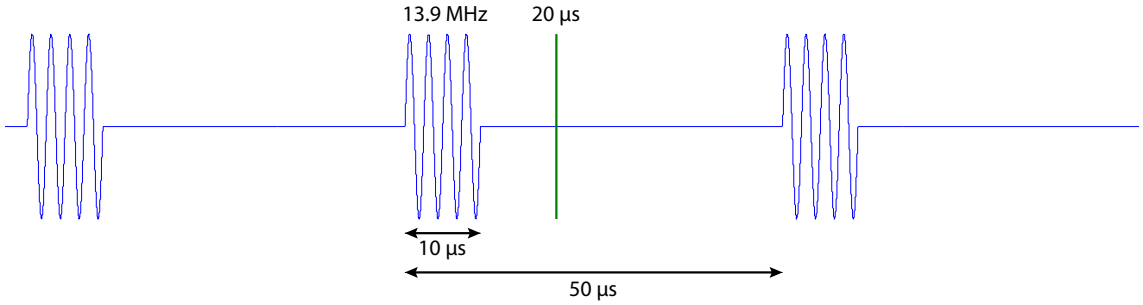

Figure 3.10: Operating signal for the rf-jet. The 20s line indicates the moment in the cycle at which the measurements where performed, unless otherwise indicated.

Figure 3.11 presents photos of the rf-plasma for both the ring electrode and the plate electrode configuration. The rf-plasma is, compared to the MW-plasma, long and thin. This is especially the case for the plate configuration, because the electric field lines are parallel to the gas flow, while for the ring electrode they are perpendicular to the gas flow. The temperatures in the center of the rf-plasma are typically between 450K and 550K [7].

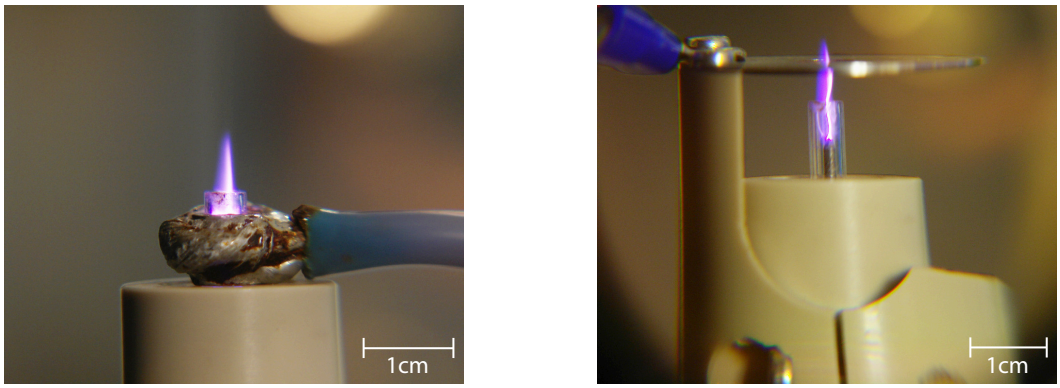

Figure 3.11: Photos of rf-plasmas, with a gas flow of 1slm He plus 2% air. Left: The ring electrode configuration. Right: The plate electrode configuration.

3.3.1 Power measurements

The power (forward minus reflected) dissipated by the plasma is calculated by subtracting the power dissipated in the matching box from the total power at constant current, see also Hofmann *et al* [17]. It is assumed that at constant RMS current (I_{RMS}) the power dissipation in the matching box remains unchanged. The current can be adjusted manually with the signal generator. The power dissipated in the matching box at a certain RMS value of the current (P_{off}), is the power determined when there is power applied to the system in the absence of a gas flow (no plasma). The total dissipated power (P_{tot}) is obtained by adding a gas flow, so that a plasma is formed. The power dissipated by the plasma (P_{plasma}) is given by,

$$P_{plasma}(I_{RMS}) = P_{tot}(I_{RMS}) - P_{off}(I_{RMS}) \tag{3.3.1}$$

Figure 3.12 shows an example of power measurements for the ring electrode. The error margin of the obtained power is estimated to be ±0.1W.

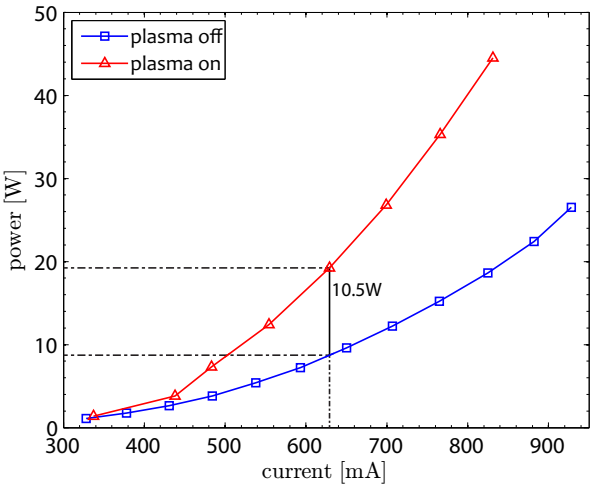

Figure 3.12: An example of power measurements for the ring electrode. Plasma off indicates the power dissipation of the matchbox and plasma indicates the power dissipation when the plasma is on, so the total power dissipation.

3.4 Vacuum system

Low pressure measurements of TALIF on Xe where required to calibrate the quenching rate of xenon at atmospheric pressure, see section 4.1.4. Therefore a vacuum system was constructed. The vacuum system is shown in figure 3.13. When performing measurements for the Xe quenching rate calibration, the vacuum system is placed in the position of the MW-plasma jet in figure 3.1.

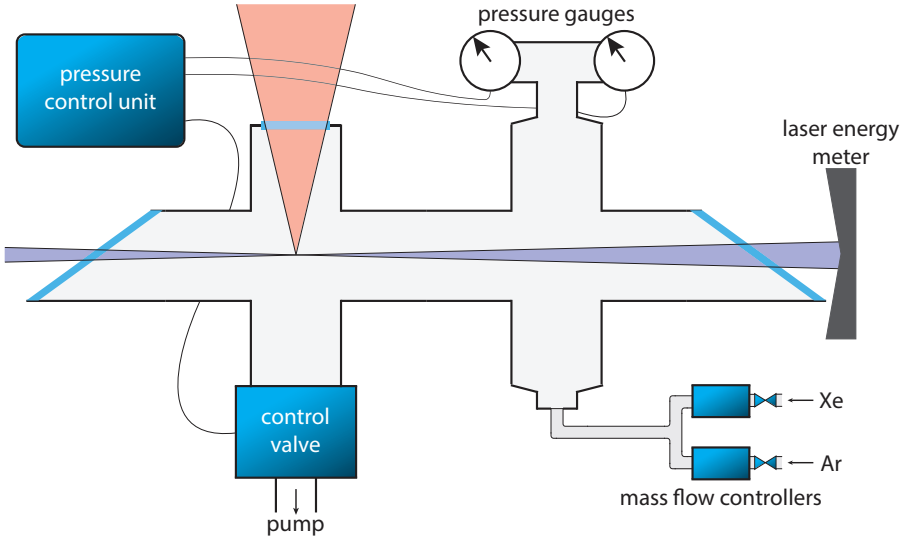

Figure 3.13: Vacuum system for low pressure measurements, with indication of the path of the laser beam and fluorescence photons.

The system was build with KF vacuum parts. It contains three quarts windows, two for the laser beam to pass, positioned under Brewster's angle to optimize the laser transmission, and one for the fluorescence signal. The pressure inside the vacuum vessel was measured with a Pfeiffer CMR271 pressure gauge or a Pfeiffer CMR363 pressure gauge with ranges up to 1000mbar and 11mbar respectively, this allowed to measure accurately the full pressure range from 1mbar up to 1bar. The gas inlet was kept constant during the measurements and was set with Brooks mass flow controllers. The pressure inside the vacuum vessel was kept constant by changing the pumping speed. This was done by means of a control valve between the vacuum vessel and the vacuum pump. The vacuum pump was a Pfeiffer Balzers Duo 016B, with a pumping speed of $16\text{m}^3/\text{h}$. A Pfeiffer RVC 300 pressure control unit was used to regulate the control valve with the pressure gauge measurement as input.

A leakdown test was performed to ensure there were no major holes in the vessel. Before gas was let in the vacuum vessel the control valve was opened maximal, resulting in a minimum pressure in the vacuum vessel of about 10^{-1}mbar. The gas density is assumed to be homogeneous in the vacuum vessel. The composition of the gas was set by the ratio of the inlet rate of the different gases.

Chapter 4

Results and discussion

This chapter is split in a microwave part and a rf part. All measurements needed for the development of the calibration method were performed with the MW-jet and the vacuum vessel, and are described in the first part. However, the part about the description of the absolute calibration, section 4.1.5, is also valid for the rf-jet.

4.1 MW-jet

In this section, a detailed description of the measurements leading up to the O-density results for the microwave jet is given. Including the low pressure measurements to determine collisional quenching rates of xenon and a description of the method which calibrates the quenching rate of xenon at atmospheric pressure, making it possible to do the calibration at atmospheric pressure.

4.1.1 Saturation

In order to measure atomic oxygen densities, saturation of the TALIF signal had to be prevented. Meaning that $n_2 \ll n_1$, where the indexes 1 and 2 represent the ground state and excited state respectively. To check for saturation the TALIF intensity is measured as a function of the laser energy. When the TALIF intensity is proportional to the square of the laser energy there is no saturation. This also means that REMPI and ASE can be neglected. The first TALIF measurements were performed with an optical filter (with a center at 850nm and a full width half maximum (FWHM) of 25nm) in front of the photomultiplier, instead of a monochromator as presented in figure 3.1. In figure 4.1 (left) the fluorescence signal has been plotted as function of the square of the laser energy for the transitions $O(2p^4\ ^3P_J \longrightarrow 3p\ ^3P_{J'})$. The transition from the $2p^4\ ^3P_2$ level seems to saturate at approximately $35(\mu J)^2$. However repeating the measurement with a neutral density filter installed in front of the photomultiplier, concludes that the non-linearity is the result of the saturation of the detection system and not of the transition. So by keeping the laser energy below $9\mu J$ the TALIF intensity of the atomic oxygen measurement is linear with the square of the laser energy under the present experimental conditions. In figure 4.1 (right) the results of the TALIF measurements with varying laser energies are presented for xenon. The results show that there is, without the use of a neutral density filter, linearity up to laser energies of $2\mu J$.

A measurement with the monochromator of the xenon spectrum indicated that with the optical filter multiple lines were measured,to the wavelength of the transition with a spectral resolution of figure 4.2. Therefore the measurements performed with the optical filter cannot be used for determining the atomic oxygen density in the plasma. The following results presented in this report are all performed with the monochromator.

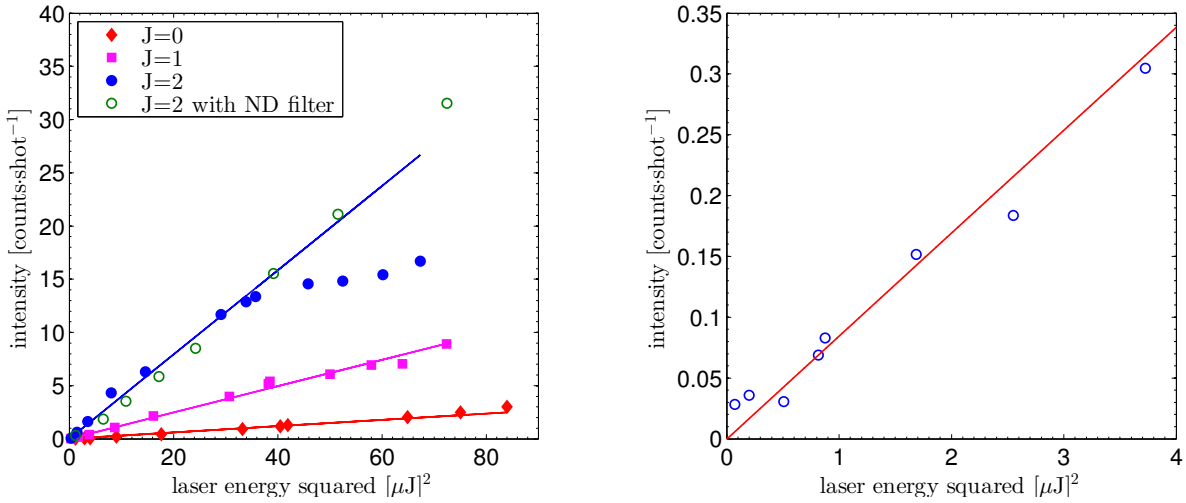

Figure 4.1: Left: Results of O-TALIF measurements on a 30W plasma with a gas flow of 6slm helium + 3.2% air, at 6mm above the top of the jet. Showing the fluorescence signal versus the squared laser energy, for the three O($2p^4\ ^3P_J \longrightarrow 3s\ ^3S_1$) transitions. Right: Fluorescence signal as function of the laser energy squared for the Xe($5p^6\,^1S_0 \longrightarrow 6p'[3/2]_2$) transition. The figure shows that the fluorescence signal is only linear with the squared laser energy for low energy levels.

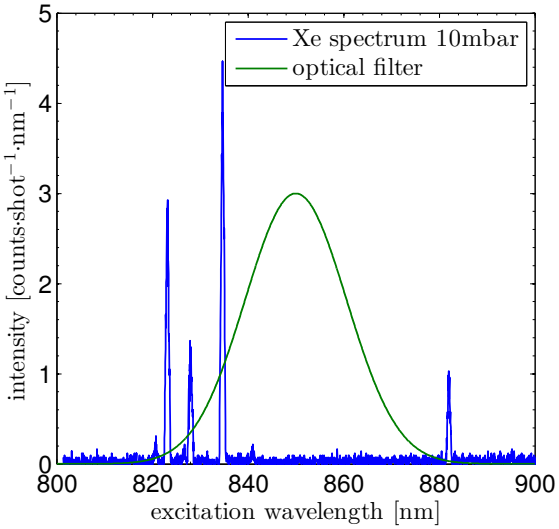

Figure 4.2: Spectrum of pure xenon at 10mbar made by a scan over the monochromator wavelength, while exciting the $5p^6\ ^1S_0$ level to the $6p\ ^2[3/2]_2$ level. The Gaussian curve represents the optical filter used for the first TALIF measurements, indicating that multiple lines where measured.

4.1.2 Gas temperature

The gas temperature of the plasma is related to the position inside the plasma. For a more accurate calibration of the atomic oxygen density, a gas temperature profile of the

plasma is needed. A gas temperature profile for the 6slm helium + 3.2% air plasma has been obtained by performing measurements on the three transitions from the ground state of atomic oxygen. The results of these measurements are presented in figure 4.3 (left).

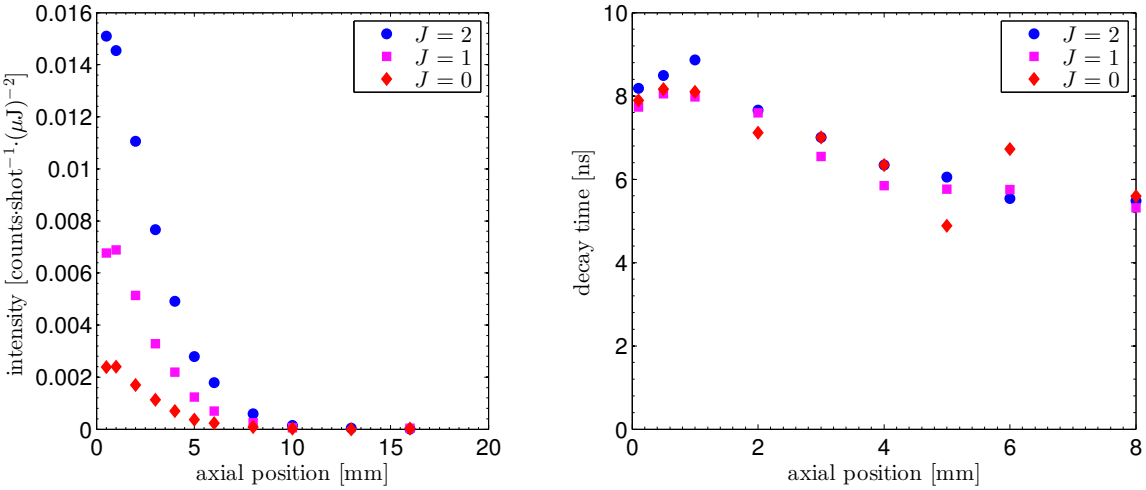

Figure 4.3: Results of O-TALIF measurements on a 30W plasma with a gas flow of 6slm helium + 3.2% air, determined at different axial positions inside the plasma. Left: Normalized fluorescence signals resulting from excitation of the three ground state levels of atomic oxygen ($2p^4\ ^3P_J$, with J =0,1 or 2 (index)). Right: The decay times of the three signals.

The gas temperature profile for the plasma can be approached by means of the Boltzmann population fraction, as mentioned in section 2.7.

From the calibration equation, equation 2.8.13, it follows that the differences in n_J for $J = 0, 1, 2$ are the result of differences in I_F, $\sigma_O^{(2)}$, and a_O. By Saxon *et al.* [18], there is shown that $\sigma_O^{(2)}$ for the transitions from the three ground state oxygen levels are equal (see also section 4.1.5). The branching ratio a_O can be expressed as A_{23}/A_2, where A_{23} is the spontaneous emission rate of the excited level to the intermediate level and A_2 is the effective de-excitation rate. The value of A_{23} is known to be equal for all three levels [13]. The values for A_2 is the reciprocal of the decay times of the measurements (figure 4.3 (right)), thus being approximately equal for all three levels. The other parameters from the calibration equation are approximately constant for the three levels and only shift the total graph in vertical direction, thus having no contribution to the slope of the curve. Because of the above, the density for the three ground state levels n_J is proportional to $I_{F,J}$, so equation 2.7.3 can be used as follows,

$$\ln\left(\frac{I_{F,J}}{(2J+1)}\right) = \frac{-E_J}{k_b T} + C_3 \tag{4.1.1}$$

Figure 4.4 (left) presents an example of a Boltzmann plot from which the gas temperature can be derived. The graph on the right gives the gas temperature profile as follows from the curves of figure 4.3. The error bars are the result of the error in the fit through the three data points.

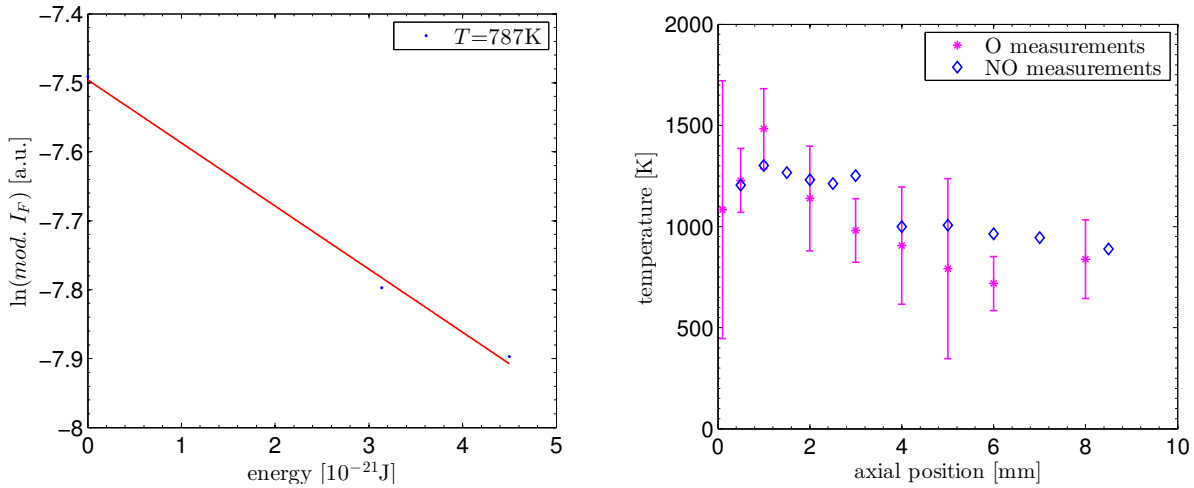

Figure 4.4: The results are obtained by using the results presented in figure 4.3. Left: linear fit through $I_{F,J}$ with J =0,1,2, to determine the gas temperature at an axial position of 5.0mm above the jet. Right: gas temperature determined for several different axial positions.

LIF measurements on NO were performed for the same MW-jet and plasma conditions by Gessel *et al* [4]. The gas temperatures determent from these measurements are also presented in figure 4.4, to compare with the data obtained from O. The gas temperatures correspond within experimental accuracy. For convenience the gas temperatures from the NO measurements were used for the absolute calibration of the oxygen density. In figure 4.5 the gas temperatures obtained by NO measurements are presented for different plasma powers. The temperatures needed for the calibration of the atomic oxygen density in the plasma are derived from figure 4.5, with an estimated accuracy of 100K.

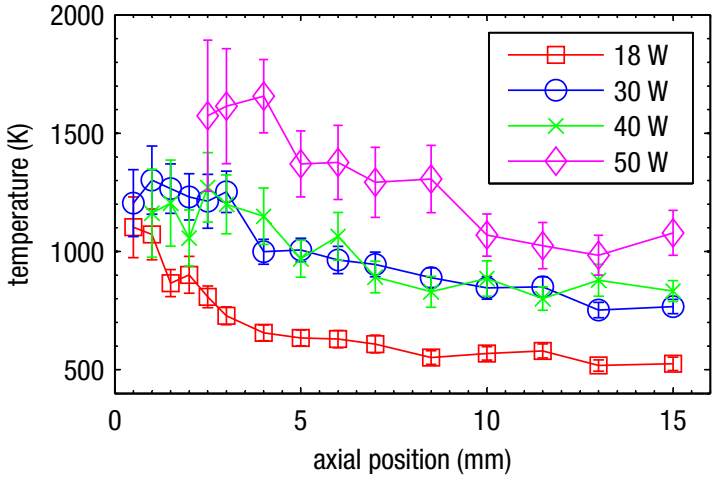

Figure 4.5: Gas temperatures as function of the axial position for the MW-jet for different plasma powers, determined by means of LIF measurements on NO by Gessel *et al* [4]. A gasflow of 6slm He + 3.2% air was used.

4.1.3 Boltzmann factor

By applying equation 2.7.1 to the calibration, equation 2.8.13, the total atomic oxygen population can be determined by only measuring one spectral line, according to

$$\sum_J n_J = \frac{\sigma_{Xe}^{(2)}}{\sigma_O^{(2)}} \frac{a_{Xe}}{a_O} \left(\frac{h\nu_O}{h\nu_{Xe}} \right)^2 \frac{I_{F,O}}{I_{F,Xe}} \frac{n_{Xe}}{f_O(T)} \tag{4.1.2}$$

where the Boltzmann factor $f_O(T)$ is dependent on the gas temperature and is therefore a function of position and plasma power. Figure 4.6 shows the Boltzmann-factor versus the gas temperature for the J=2 ground state level of atomic oxygen. The figure indicates that in the temperature range of the microwave plasma the inaccuracy of the temperature profile results in a maximum inaccuracy in the Boltzmann factor of 3%. Although the sensitivity increases for lower temperatures, the accuracy of the temperature also increases, keeping the uncertainty in the Boltzmann-factor limited.

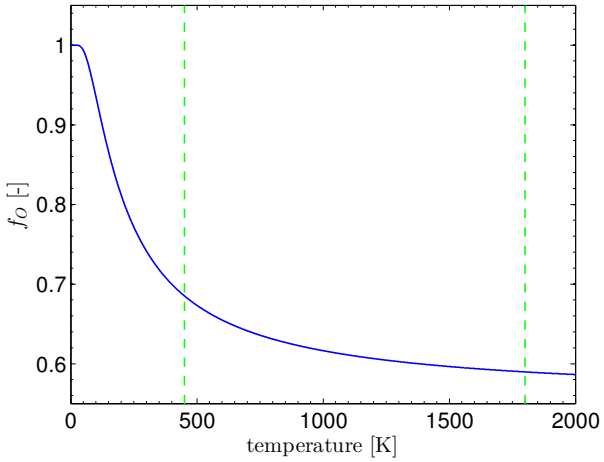

Figure 4.6: Boltzmann-factor for the J=2 ground state level of oxygen. Dashed lines indicate the gas temperature range of the microwave plasma.

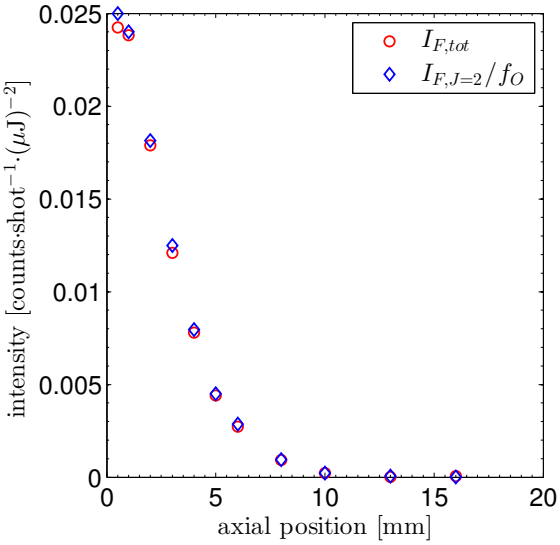

Figure 4.7: Comparison of the total atomic oxygen density calculated from the sum of the three signals presented in figure 4.3(left) and the density calculated from only the J=2 signal (figure 4.3(left)) and the corresponding Boltzmann-factor.

By using the measurement results from figure 4.3 it was already shown that the gas temperature, which was derived by means of the Boltzmann plot, was consistent with

the gas temperature determined by the LIF measurements on NO, section 4.1.2. Furthermore the same measurement results can be used to compare the total fluorescence intensity from the ground state atomic oxygen, by adding the three fluorescence signals from J=0,1,2, with the total intensity from only the J=2 signal and corrected with the Boltzmann-factor, figure 4.7. These results show that the ground state atomic oxygen in the helium-air plasma does exhibit a thermal population distribution, and therefore measuring only the J=2 transition is sufficient to determine the total O density with a good accuracy.

4.1.4 Collisional quenching rates

To determine the quenching rate of atomic oxygen and xenon, knowledge of the natural lifetimes and quenching coefficients for the significant species are necessary (equation 2.6.1). The natural lifetimes and quenching coefficients relevant to this report are listed in table 4.1 and table 4.2 respectively.

Table 4.1: Natural lifetimes for O($3p^3P_J$) atoms and Xe(6p'$[3/2]_2$) atoms.

Excited state	Natural lifetime $[ns]$
O($3p^3P_J$)	34.7 ± 1.7 [8]
Xe(6p'$[3/2]_2$)	40.8 ± 2.0 [8]

Table 4.2: Two-particle quenching coefficients for O($3p^3P_J$) atoms (left) and Xe(6p'$[3/2]_2$) atoms (right).

Reagent	Quenching coefficient $[10^{-10} cm^3 s^{-1}]$
He	0.017 ± 0.002 [8]
N_2	5.9 ± 0.6 [19]
O_2	9.4 ± 0.5 [8]

Reagent	Quenching coefficient $[10^{-10} cm^3 s^{-1}]$
He	5.7 ± 0.6 [20]
Ar	2.5 ± 0.3 [20]
Xe	3.6 ± 0.4 [8]

The number densities of a gas component i necessary to calculate the quenching rate are obtained according to Dalton's law

$$n_i = \frac{\phi_i}{\phi_{tot}} n_{tot} \simeq \frac{\phi_i}{\phi_{tot}} \frac{p}{k_b T} \tag{4.1.3}$$

where ϕ denotes the gas flow and k_b is the Boltzmann constant.

The pure optical branching ratios (A_{ik}/A_i, $Q_i = 0$) for the atomic oxygen transition and for the xenon transition are given by Niemi et al. [8], and are 1 and 0.733 respectively.

Collisional quenching rates O

The effective branching ratio, a_O, can be expressed by equation 4.1.4,

$$a_{23} = \frac{A_{23}}{A_2} = \frac{A_{23}}{\tau_0^{-1} + Q} \tag{4.1.4}$$

The effective de-excitation rate A_2 can be determined by means of a fit of the intensity decay as was presented in figure 3.5, which yielded A_2=2.2·10^{8}s^{-1}. With $A_{23} = 3.22 \cdot 10^7 s^{-1}$ the branching ratio a_O is 0.14.

The quenching rate and effective de-excitation rate for oxygen can also be calculated using equations 2.6.1 and 2.6.3, by using the values for $\tau_{0,O}$ and $k_i^{(1)}$ listed in tables 4.1 and 4.2 respectively. For the atomic oxygen measurements the helium and air densities are calculated by applying the temperature function as described in section 4.1.2. The O_2 and N_2 densities are found by multiplying the air density with the corresponding fraction of that component in air (1 represents 100%), which are 0.21 and 0.78 respectively. Calculating the branching ratio for the same measurement for which the A_2 was determined by means of a fit (6slm He + 3.2% air), a value for a of 0.14 can be found. So two different methods can be used to determine the branching ratio for atomic oxygen.

Collisional quenching rates Xe

The calculated de-excitation rate for xenon does not match with the de-excitation rate measured at atmospheric pressure due to three body quenching, as will be indicated later-on. To check the quenching coefficients for xenon as presented in table 4.2, low pressure TALIF measurements were performed for different gas compositions. The low pressure measurements were performed with the vacuum vessel as described in section 3.4. The resulting Stern-Volmer plot is presented in figure 4.10 and the corresponding quenching coefficients are presented in table 4.3.

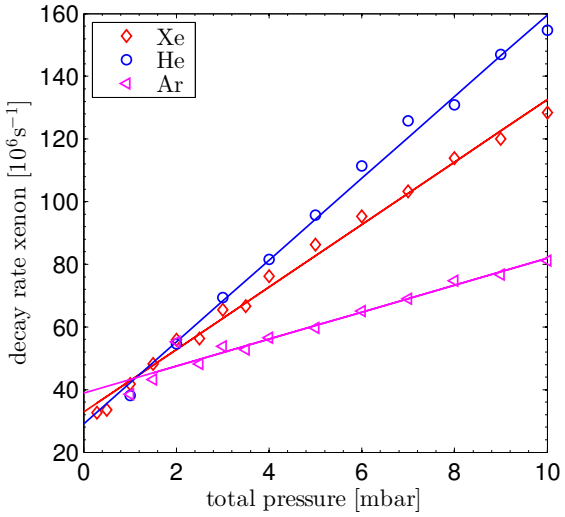

Figure 4.8: Stern-Volmer plot for the gases pure xenon, Xe+He mixture and Xe+Ar mixture.

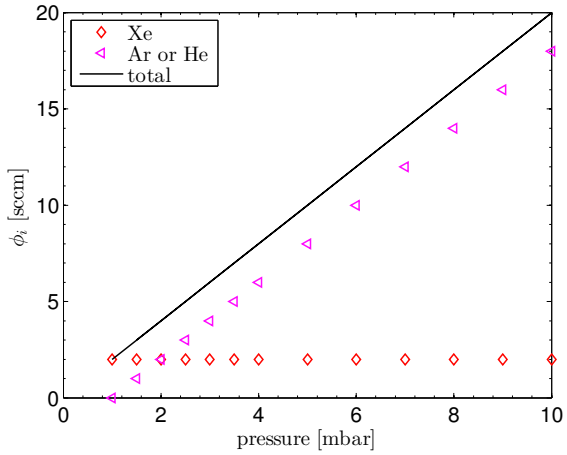

Figure 4.9: Gas flows (ϕ) during low pressure TALIF measurements to determine two particle quenching coefficients. The gas flows were controlled by mass flow controllers.

During the pure xenon measurements the pressure inside the vacuum vessel was increased by letting more xenon in the vessel. The xenon self-quenching coefficient k_{Xe} follows from the derivative of the equation for the effective de-excitation rate, equation 2.6.3, applied to pure xenon quenching,

$$\frac{dA}{dp} = \frac{k_{Xe}}{k_b T} \tag{4.1.5}$$

The quenching coefficient k_i of the xenon quenching with gas i (Ar or He) is not determined in the same manner as the xenon self-quenching coefficient. During the measurements the pressure inside the vacuum vessel was increased by increasing the flow of gas i(as is indicated in figure 4.9), keeping the number density of xenon inside the vacuum vessel constant, according to

$$n_{Xe} = \frac{\phi_{Xe}}{\phi_{Xe} + \phi_i} \frac{p}{k_b T} \tag{4.1.6}$$

Which can be simplified to

$$\frac{p}{\phi_{tot}} = C \tag{4.1.7}$$

Where $\phi_{tot} = \phi_{Xe} + \phi_i$ and C is a known constant with unit [Pa$\cdot$ min$\cdot$cm^{-3}]. By doing this the xenon partial pressure, and thus the xenon self-quenching, is constant. This means that the decrease in the measured decay time is only due to the quenching with gas i.

The equation for the decay rate of xenon becomes,

$$A = \frac{1}{\tau_0} + \frac{\phi_{Xe}}{\phi_{tot}} \frac{k_{Xe}}{k_b T} p + \frac{\phi_i}{\phi_{tot}} \frac{k_i}{k_b T} p \tag{4.1.8}$$

The quenching coefficient can be determined by taking the derivative of equation 4.1.8, what leads to,

$$\frac{dA}{dp} = \frac{k_i}{k_b T} \tag{4.1.9}$$

Note that extrapolations of the linear fits in figure 4.10 to a pressure of 0mbar only yields the natural lifetime of xenon for the measurement with pure xenon.

Table 4.3: Two-particle quenching coefficients for Xe(6p'[3/2]$_2$) atoms determined by low pressure TALIF measurements in the vacuum vessel.

Reagent	Quenching coefficient $[10^{-10}\mathrm{cm}^3\mathrm{s}^{-1}]$
He	5.4 ± 0.6
Ar	1.8 ± 0.4
Xe	4.1 ± 0.4

The quenching coefficients presented in table 4.3 correspond to the quenching coefficients presented in table 4.2 within experimental accuracy. The natural lifetime for xenon which follows from the Stern-Volmer plot, (30 ± 5)ns, does not correspond to the natural lifetime presented in table 4.1. A possible explanation is that there is a systematic error in the pressure, which would shift the curve effecting the natural lifetime, but would not influence the slope of the curve effecting the quenching coefficient. The quenching coefficient for argon is lower than the quenching coefficient for helium, because the TALIF intensity will be higher when the quenching is lower, the calibration measurements with xenon are performed in argon. The use of argon for the xenon measurements has no influence on the calibration of the helium-air plasma, because the calibration equation takes collisional quenching into account.

The calculated de-excitation times do not correspond with the measured de-excitation times at atmospheric pressure, because the quenching coefficients were determined for pressures below 10mbar, for which there is only two particle quenching. Figure 4.10 presents relative effective de-excitation rates determined by intensity measurements, indicating that at atmospheric pressure three particle quenching occurs. Thus resulting in a higher quenching rate and a lower effective de-excitation rate. Because the quenching rate at atmospheric pressure could not be determined by means of an exponential fit, an alternative method has been investigated, section 4.1.4.

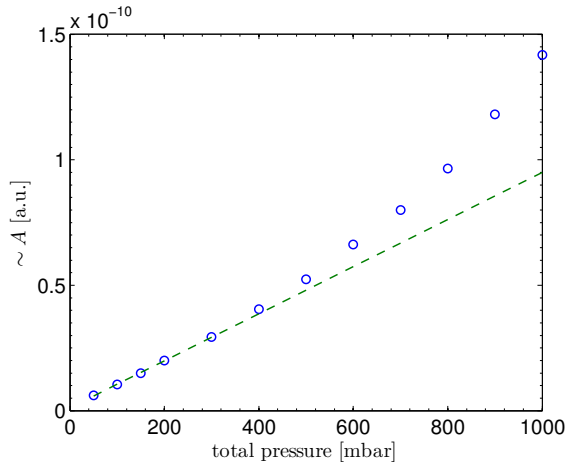

Figure 4.10: Stern-Volmer plot presenting a non-linear relation for higher pressures. Xe+He gas mixture with a constant helium flow of 4sccm and a constant xenon flow of 1sccm.

The relation between the de-excitation rate and the pressure as presented in figure 4.10 was derived from equation 2.8.11. By realizing that for a constant gas flow into the vacuum vessel the variation in intensity I_F is only dependent on the density n_0, through the pressure, and the branching ratio a_{23}, through the de-excitation rate A, the following relation can be derived,

$$A = \gamma \frac{p}{I_F} \tag{4.1.10}$$

where γ is an unknown constant. The results presented in figure 4.10 are the values for p/I_F.

Calibration branching ratio xenon at atmospheric pressure

The branching ratio of xenon a_{Xe} needed for the absolute O density calibration is dependent on the unknown collisional quenching rate of xenon at atmospheric pressure. Because this collisional quenching rate is not known, a_{Xe} at atmospheric pressure is determined by means of the signal intensity. For this approach equation 4.1.11 has been derived in the same manner as equation 4.1.10, but it is independent on the pressure because the partial pressure of xenon was kept constant. c Is a constant composed of atomic and experimental constants and is independent on the pressure.

$$I_{F,Xe} = c \cdot a_{Xe} \tag{4.1.11}$$

The calibration of the branching ratio at atmospheric pressure needs two intensity measurements. One at low pressure, for which the decay time and thus the de-excitation rate and branching ratio can be determined, and a second measurement at atmospheric pressure. Dividing equation 4.1.11 for atmospheric pressure with the same equation for low pressure, yields the following relation,

$$a_{Xe}^{1000mbar} = \frac{I_{F,Xe}^{1000mbar}}{I_{F,Xe}^{2mbar}} \cdot a_{Xe}^{2mbar} \tag{4.1.12}$$

This method can be applied to the 834.68nm transition, but it can also be applied to the 823.16nm transition, which occurs after quenching of the 6p $^2[3/2]_2$ level to the 6s $[3/2]_2$ level. The advantage of this transition is that it has a higher intensity at atmospheric pressure than the intensity from the 834.68nm transition, as a result of the strong quenching rate at atmospheric pressure. Because the spontaneous emission coefficient of this transition is not known, the low pressure calibration has to be performed with the 834.68nm transition.

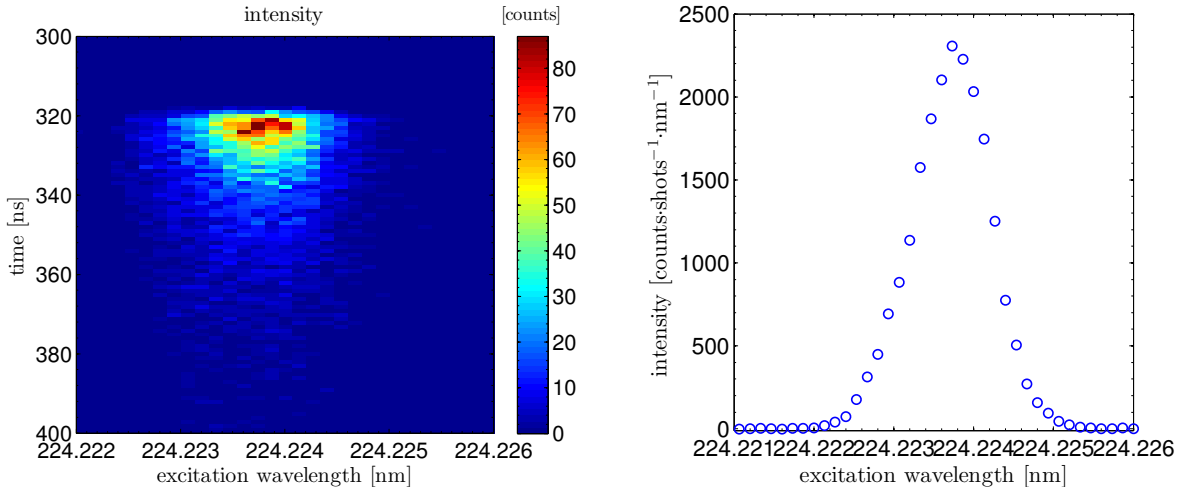

Figure 4.11: Left: Time and wavelength resolved TALIF signal of a pure xenon gas at 2mbar, inside a vacuum vessel. Right: Time integrated signal to determine I_F.

The two measurements for the 834.68nm transition were performed immediately after each other, to minimize the effect of varying parameters on the measured values. The result of the measurement at 2mbar is presented in figure 4.11 (left). $I_{F,Xe}$ is determined by integrating the wavelength resolved signal, figure 4.11 (right). The effective de-excitation rate A_2 is obtained from a fit (as described in section 3.1) through the time resolved signal, figure 4.12. For this measurement a de-excitation rate of $(7.0 \pm 0.3)\cdot 10^7 \mathrm{s}^{-1}$ was obtained. A value for A_{23} of $1.80 \cdot 10^7 \mathrm{s}^{-1}$ can be found by dividing the pure optical branching ratio for xenon, 0.733 [8], by the natural lifetime of xenon, table 4.1. This yields a branching ratio for xenon at 2mbar for the 834.68nm transition of 0.26 ± 0.02 (note that the branching ratio has no unit).

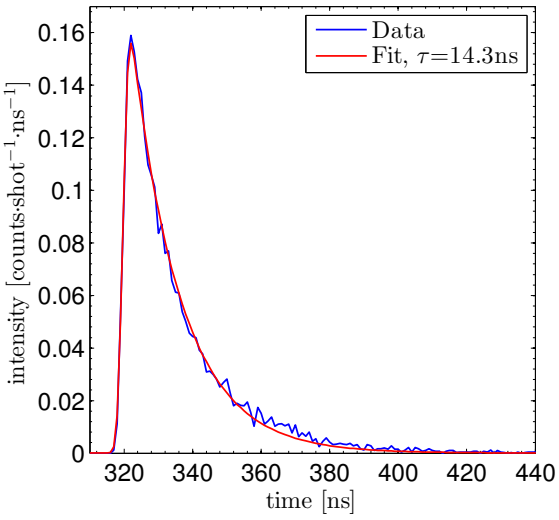

Figure 4.12: Wavelength integrated TALIF signal, with fit to determine the effective de-excitation rate of xenon at 2mbar.

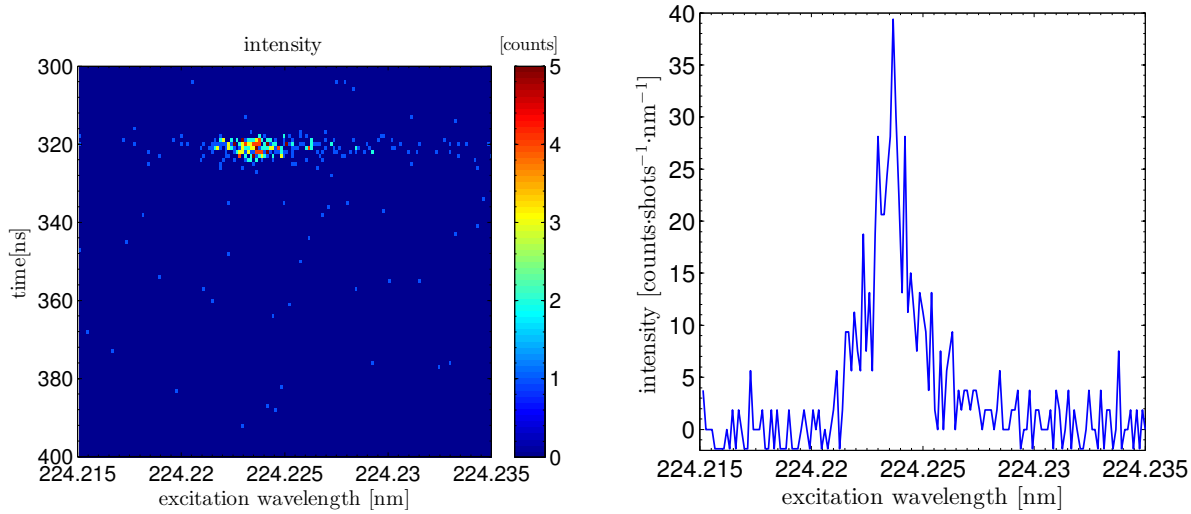

Figure 4.13: Left: Time and wavelength resolved TALIF signal of argon plus xenon gas mixture at 1000mbar, inside a vacuum vessel. Right: Fit through the time integrated signal to determine I_F.

The results for the measurement for the 834.68nm transition at 1000mbar are presented in figure 4.13, again $I_{F,Xe}$ has been determined by integrating the wavelength resolved signal. Comparing figures 4.11 (right) and 4.13 (right) shows the broadening of the signal as a result of an increase in pressure.

Equation 4.1.12 gives an effective branching ratio for the xenon transition of 834.68nm at atmospheric pressure, a_{Xe}, of $(8 \pm 2)\cdot 10^{-3}$. Applying the method to the 823.16nm transition results in an branching ratio a^Q_{Xe} of $(13 \pm 6)\cdot 10^{-3}$. These values for the branching ratios are only valid as long as the argon-xenon gas mixture is used in the proportion 500:1 sccm respectively.

4.1.5 Absolute calibration

In this section the absolute calibration of the atomic oxygen density is described by means of an example. The data which is used in this example was obtained from a measurement performed on a 30W microwave jet plasma, 6slm He + 3.2% air, at an axial position of 5mm above the jet. The estimated gas temperature at 5.0mm above a 30W microwave jet is (940±50)K.

In the following subsections the methods in which the parameters of the calibration equation, equation 4.1.2, were obtained are described.

The error in the atomic oxygen density was determined by means of the general equation

$$\delta q = \sqrt{(\frac{\partial q}{\partial x_1}\delta x_1)^2 + ... + (\frac{\partial q}{\partial x_m}\delta x_m)^2} \tag{4.1.13}$$

where $x_1, x_2, ..., x_m$ are the measured parameters with uncertainties $\delta x_1, \delta x_2, ..., \delta x_m$ and $q = f(x_1, x_2, ..., x_m)$.

Number density n

The number densities of a gas component i are obtained according to Dalton's law 4.1.3. For the plasma measurements the helium and air densities are calculated as discribed in section 4.1.4. The densities for the three components at an axial position of 5.0mm are listed in table 4.4.

Table 4.4: Number densities for a 30W helium + 3.2% air plasma at 5.0mm above the center of the jet.

Reagent	Number density $[10^{24}\mathrm{m}^{-3}]$
He	7.5 ± 0.9
N_2	0.19 ± 0.03
O_2	0.050 ± 0.007

For the xenon measurements at atmospheric pressure, a pressure of (1.0 ± 0.05)bar and a temperature of (300 ± 3)K were used. With a xenon flow of (5.0 ± 0.1)sccm and an argon flow of (2.5 ± 0.3)slm equation 4.1.3 yields a n_{Xe} of $(4.8 \pm 0.6)\cdot 10^{22}\mathrm{m}^{-3}$.

Two-photon excitation cross section

The work of Niemi et al. [8] gives a value of 1.9 for the fraction $\sigma^{(2)}_{Xe}/\sigma^{(2)}_{O}$ with an estimated uncertainty of $\sim 20\%$. Furthermore Saxon et al. [18] gives calculated values for the two-photon absorption cross sections for transitions from the O(^3P) ground state. The, for this research interesting, cross sections for atomic oxygen are presented in table 4.5, where $\sigma^{(2)}_{JJ'}$ is the fine-structure cross sections for two-photon absorption.

The two-photon excitation cross section for the three transitions from ground state can be calculated by,

$$\sigma^{(2)}_{J} = \sum_{J'} \sigma^{(2)}_{JJ'}$$

This yields a $\sigma^{(2)}_0$,$\sigma^{(2)}_1$ and $\sigma^{(2)}_2$ of $23.9 \cdot 10^{-47}\mathrm{cm}^4\mathrm{s}$. So according to this work, they are equal for all three transitions.

Table 4.5: $\sigma^{(2)}_{JJ'}$ in units of $10^{-47}\mathrm{cm}^4\mathrm{s}$.

$J_{initial}$	J'_{final}	$3p^3P$	$J_{initial}$	J'_{final}	$3p^3P$	$J_{initial}$	J'_{final}	$3p^3P$
0	0	13.415	1	0		2	0	2.101
0	1		1	1	16.042	2	1	4.738
0	2	10.507	1	2	7.880	2	2	17.093

Normalized fluorescence signal I_F

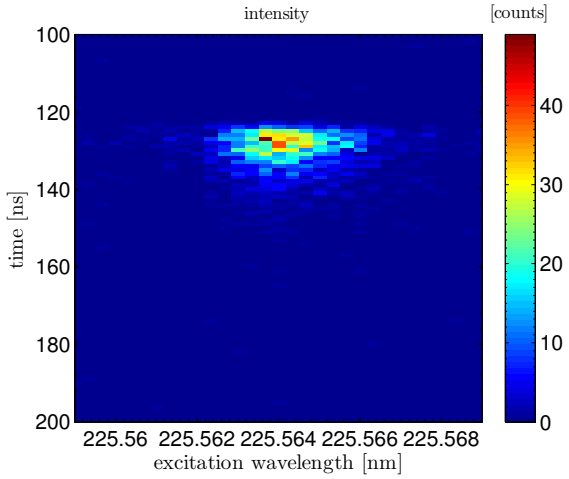

Figure 4.14: Time and wavelength resolved TALIF signal of a microwave jet plasma; 6slm He + 3.2% air, 30W microwave power, measured at an axial position of 5.0mm above the jet.

Figure 4.14 presents the time and wavelength resolved TALIF signal which is the result of excitation of the $J = 2$ ground state level of atomic oxygen. The time and spectral integrated photomultiplier signal, S_{PMT}, is obtained by integration of the wavelength resolved TALIF signal.

The normalized fluorescence signal I_F is obtained by dividing S_{PMT} by the mean of the square of the laser energy. For this measurement a S_{PMT} of (0.57 ± 0.05) counts·shot^{-1} is obtained, which results, with a mean laser energy of (14 ± 2) μJ, in an $I_{F,O}$ of $(29 \pm 7) \cdot 10^{-4}$ counts·shot$^{-1} \cdot (\mu\text{J})^{-2}$.

The normalized fluorescence signals for the xenon measurements, $I_{F,Xe}$, is obtained in the same way as that of atomic oxygen. For this measurement an $I_{F,Xe}$ of $(48 \pm 6) \cdot 10^{-4}$ counts·shot^{-1}·$(\mu\text{J})^{-2}$ is obtained for the 823.16nm transition, resulting from a laser energy of (11 ± 1) μJ. The error in I_F follows from the repeatability of three identical measurements.

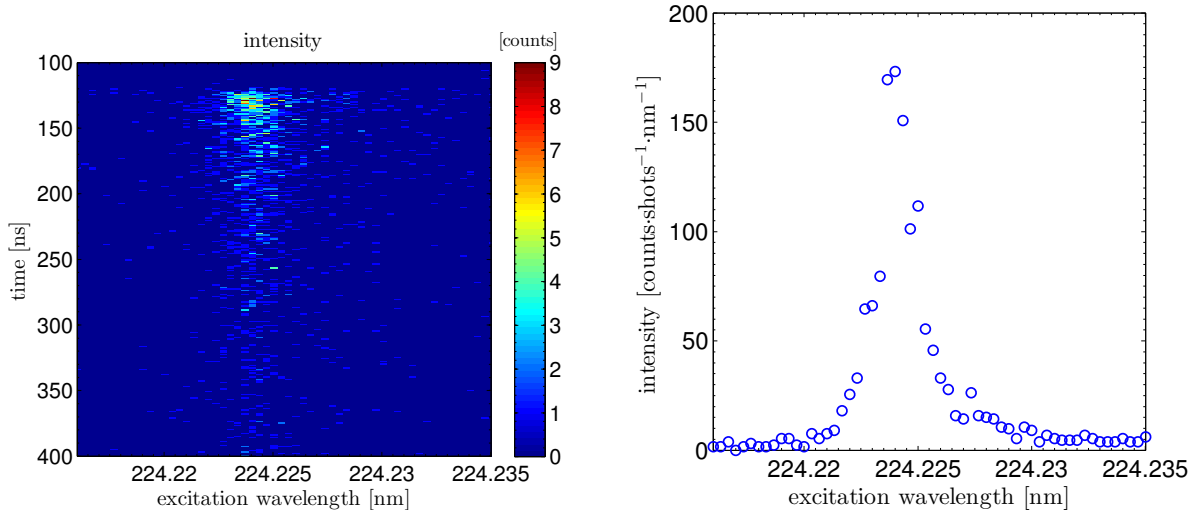

Figure 4.15: Left: The time and wavelength resolved TALIF signal for a xenon calibration measurement; 2.5slm Ar + 5sccm Xe, measured at an axial position of 0.5mm above the jet. Right: time integrated TALIF signal.

Atomic oxygen density n_O

The remaning parameters are the Boltzmann-factor for a temperature of 940K, which is (0.62 ± 0.01), the photon energy for the laser excitation of the O and Xe transitions which can be derived from figure 2.5, and the branching ratios for O and Xe as described by section 4.1.4, which gives an a_O of (0.14 ± 0.04) and a a_{Xe}^Q of $(13 \pm 6)\cdot 10^{-3}$. Filling in all parameters in equation 4.1.2 gives a total atomic oxygen density of $4.9 \cdot 10^{21}\mathrm{m}^{-3}$ with an uncertainty of 60%.

4.1.6 Spatial resolved O-density

A spatially resolved O-density profile of the MW-plasma, as presented in figure 4.16, can be obtained by moving the MW-jet both in radial and axial direction. The profile consists of 108 measurement point, nine in radial direction at 0, ±1, ±2, ±3 and ±4mm and twelve in axial direction at 0.1, 0.5, 1.0, 2.0, 3.0, 4.0, 5.0, 6.0, 8.0, 10.0, 13.0 and 16.0mm.

The 2D plasma profile of the O-density shows that the O production is focused in the center of the plasma close to the pin electrode, where the electric field line density and thus the electron density are the highest. This could be an indicates that reaction 2.3.1:

$$O_2 + e \rightarrow 2O + e$$

is indeed the most dominant reaction for the production of atomic oxygen in the microwave plasma.

Atomic oxygen densities of $3.1{\cdot}10^{22}\mathrm{m}^{-3}$ are reached in the core of the plasma. The concentration of molecular oxygen O_2 in a 6slm helium flow + 3.2% air at atmospheric pressure and a temperature of 300K is approximately $1.6{\cdot}10^{23}\mathrm{m}^{-3}$. So at least 10% of the O_2 in de gas flow is dissipated in the core of the plasma; Note the many chemical

reaction mentioned in section 2.3 which influence the atomic oxygen concentration, thus the 10% O_2 dissipation must be an absolute minimum. Reuter *et al* [1] measured O densities in the effluent of a kINPen just above the nozzle of the jet of $2.75{\cdot}10^{21}\mathrm{m}^{-3}$, using the same diagnostic method. An argon flow of 5slm + 1% pure O_2 was used and the rf-jet was operated in open air. There are many differences and the plasma power of the kINPen plasma is not known, but it gives an indication that the O-densities found for the microwave jet are of the right order.

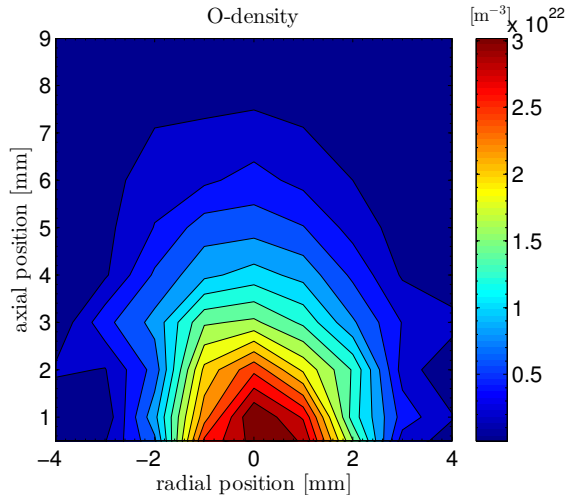

Figure 4.16: Radial and axial plasma profile for a 30W, 6slm helium + 3.2% air plasma.

4.1.7 O-density dependence on air concentration and plasma power

To investigate the influence of the air concentration added to the gas flow on the atomic oxygen density in the plasma, several measurement series where performed with different added air concentrations (0.0 - 6.3%) for different axial positions; the radial position was zero. For each of these measurement series the plasma power was adjusted to 30W. In figure 4.17 the fluorescence intensity is presented for a measurement for which no air was added to the gas flow. Because an intensity was measured, there must be atomic oxygen present. This can only be the result of entrainment of the surrounding air, with a maximum entrainment at 2mm above the jet. A change in air concentration in the plasma would influence the calculation of the oxygen branching ratio, changing the calibrated O-density. However, the O-density calculated from this pure helium signal is negligible small compared to the O-density measurements with higher concentration, figure 4.17. Furthermore in section 4.1.4 it was shown that hte measured and calculated a_O was the same, this would not be the case if air entrainment played an important role. Reuter *et al* [1] also mentioned that although the air entrainment is detectible, it is irrelevant for most applications. The air entrainment is assumed to be irrelevant for the MW-jet measurements.

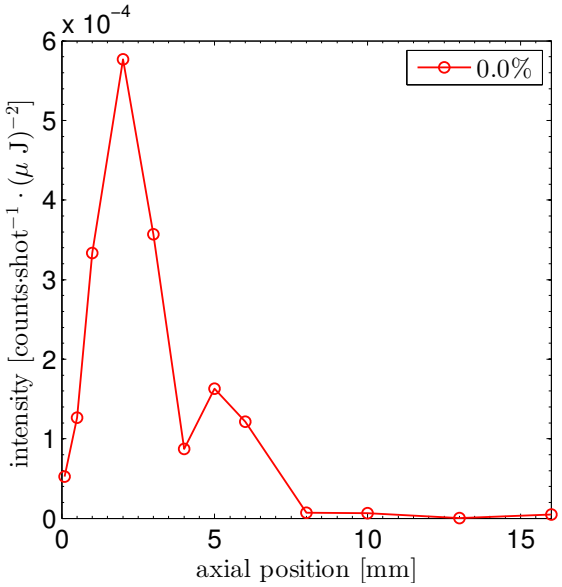

Figure 4.17: TALIF intensity for a 30W helium plasma with a helium flow of 6slm. The 0.0% in the legend indicates that there was no air added to the gasflow.

Figure 4.18 shows that there are two changes to the plasma when the added air concentration increases. First the O-density in the core of the plasma increases, possibly because the reaction probability of the free electrons with O_2 and N_2 increases, because of an increase in O_2 and N_2 concentrations. This would also explain the shrinking of the plasma, which would be the result of the drop in energetic free electrons further away from the nozzle.

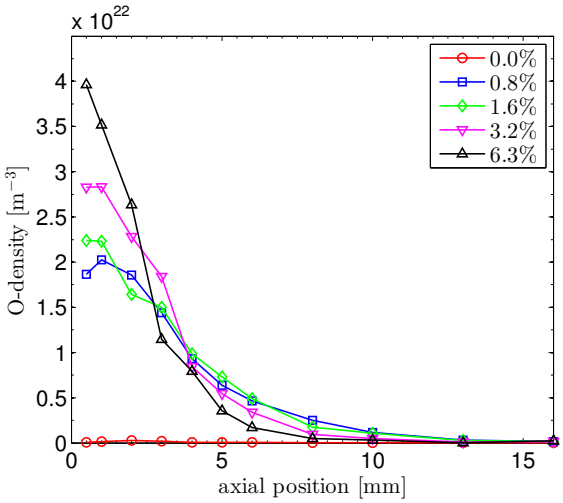

Figure 4.18: Oxygen density for several different air concentrations added to the 6 slm helium plasma. The plasma power was adjusted to 30W for each added air concentration.

The influence of the plasma power on the O-density in the plasma was investigated by performing TALIF measurements on plasmas with different powers in the range of 20-56W, while keeping the added air concentration constant on 3.2%. The results are presented in figure 4.19. With an increase in plasma power from 20W to 56W the O-density in the core of the plasma increases only slightly, while the plasma size increases approximately 3mm in the axial direction. Possible explanation is that the O_2 molecules

are almost all dissociated, as a result of which the mean free path of the free electrons becomes larger, increasing the plasma size. A different explanation could be that there is an equilibrium between reactions producing oxygen and reactions consuming oxygen.

Comparing the 31W measurement from figure 4.19, the 3.2% air measurement from figure 4.18, and the O-densities presented on the axial axis in figure 4.16, which have approximately the same measurement conditions but were performed on different days, indicates that the reproducibility of the measurement method is within approximately 20%.

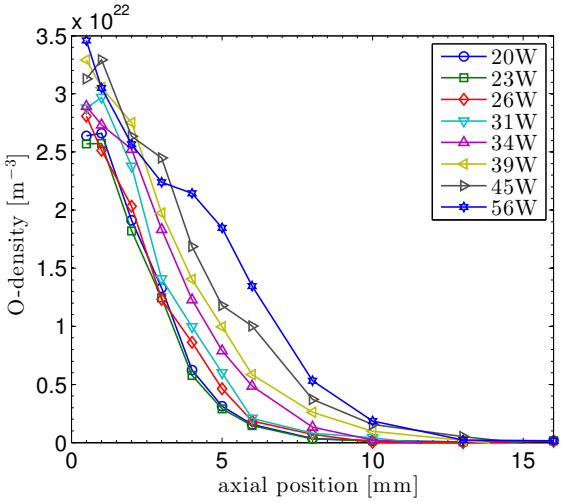

Figure 4.19: Oxygen density for several different plasma powers of a 6slm helium + 3.2% air plasma.

4.1.8 Conclusion MW-measurements

A 2-dimensional profile of the O-density of the microwave plasma has been obtained. Maximum atomic oxygen densities are obtained in the core of the plasma, where the electron density is the largest. The maximum densities for standard conditions used in this work (30W, 6slm He+3.2% air) is $3.0{\cdot}10^{22}\mathrm{m}^{-3}$. Increasing air concentration leads to increasing O densities in the core of the plasma. Increasing power rather increases the O density in the far effluent compared to the core of the density. A dissociation degree of 50% can be found for a gas temperature in the core of 1500K.

The TALIF measurements are reproducible within 20%, the uncertainty in the atomic oxygen density, determined by calculating the oxygen branching ratio, is however 60% as a result of the uncertainties in the many variables used for the calibration. Because of the high gas ow through the microwave jet, the air entrainment of ambient air into the plasma is low and can be neglected.

4.2 RF-jet

In this section the results of the atomic oxygen densities of both the ring and plate configurations are presented. The xenon measurements for calibration of the atomic oxygen density in the rf plasma were done in the same manner as the measurements for the microwave jet. So the xenon measurements where performed using the tube of the microwave jet, as is described in section 3.2.

In the previous sections there was described how the effective de-excitation rate A_2 can be determined in two different ways, by fitting the decay of the wavelength integrated TALIF signal and by calculation using quenching coefficients. It was also shown that both methods give approximately the same result for the microwave jet. For the rf-jet the TALIF signal is much weaker than the signal for the microwave at equal axial positions and can not be fitted accurately to obtain A_2, so effective de-excitation rate for the rf-jet can only be determined through calculation.

The plasma power measurements deviates a bit from previous performed power measurements on the same jet. The cause of this was most likely a damaged wire between the jet and the matchingbox. Although the power measurements were stable, the calculated plasma power is most likely not the absolute plasma power. However, the plasma powers are assumed to be relatively correct, meaning that an increase in calculated power is indeed an increase in actual power and that equal powers for different plasma conditions are indeed equal.

4.2.1 Background

One of the differences with the microwave jet is that the background of a rf-plasma is not "constant". The background radiation with a wavelength of 844.62nm pulsates with 13.9MHz during the 10μs of the cycle when there is a rf-operating signal. During these 10μs each time a plasma is formed oxygen atoms are being excited and consequently will de-excite, resulting in a signal even when there is no plasma between the pulses. This pulsating background (figure 4.20) makes it difficult to perform TALIF measurements on atomic oxygen during these 10μs.

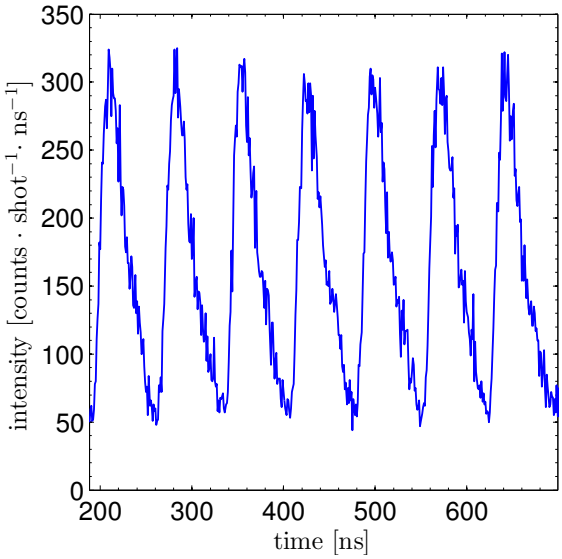

Figure 4.20: Pulsating background of 3.5W rf-plasma with a flow of 1slm argon + 2% air.

TALIF measurements were performed on atomic oxygen during several moments spread over the 50μs cycle to determine how the atomic oxygen concentration varies during an interval of one cycle. The measurements during the 10μs that the signal was pulsating were performed in the time interval when the background was the lowest. The results are presented in figure 4.21.

Both data series in figure 4.21 were performed with the same settings, however reflections of the laser beam occurred while measuring the series with the higher intensity. Correcting for this is difficult especially when there is a pulsating background involved. The laser reflections and the pulsating background cause the measurements in the first 10 μs to be unreliable. However the measurements after the first 10 μs indicate that there is no significant change of the atomic oxygen density in the period when there is no plasma. To confirm that the change in atomic oxygen concentration is indeed not significant, the set-up was adjusted so that there were no more reflections of the laser beam, which resulted in a lower intensity. New measurements were performed, resulting in the second series presented in figure 4.21. From these measurements can be assumed that the O-density is constant during the whole cycle.

All the following measurements were performed with a delay time of 20μs, which is indicated in figure 3.9.

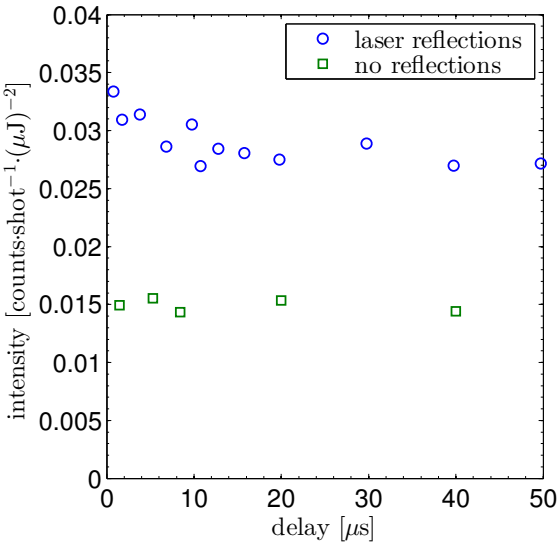

Figure 4.21: The intensity of TALIF on atomic oxygen as function of the delay time. A delay time of 20μs corresponds with the 20μs indication in figure 3.9.

4.2.2 Temperature

LIF measurements on NO were performed for the same rf-jet and plasma conditions by Gessel *et al* [4]. The results are presented in figure 4.22. These measurement results have been used to calibrate the atomic oxygen densities of the rf-plasmas. The measurements have been taken during different measurement campaigns and care has been taking to work for the same plasma conditions.

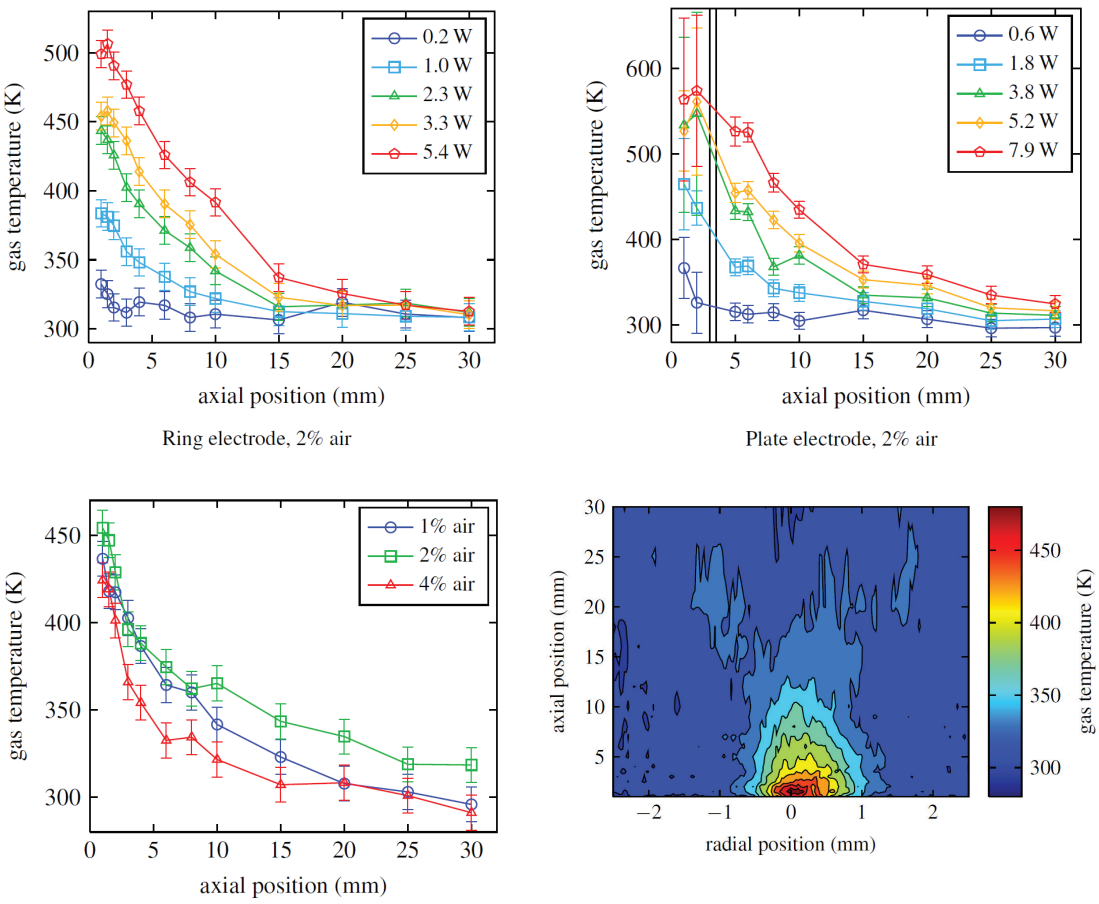

Figure 4.22: The gas temperatures of the rf-plasma, determined by LIF measurements on NO. The lower two temperature profiles were obtained with the ring electrode; the left one for a 3.5W plasma, the right one for a 3.7W, 2% air plasma.

4.2.3 Axial dependence

The atomic oxygen density as function of the axial position, for a 3.5W plasma with a 2% added air concentration, for both the ring and plate electrode configuration are presented in figure 4.23. The radial position is kept zero. These graphs show that in case of the ring electrode the highest atomic oxygen density can be found closest to the glass tube, $1.5 \cdot 10^{22}\mathrm{m}^{-3}$ at an axial position of 1mm, while the the highest atomic oxygen density in case of the plate electrode can be found between the plate and the glass tube, $1.0 \cdot 10^{22}\mathrm{m}^{-3}$ at an axial position of 1.5mm. In case of the ring electrode the electric field line density is the highest in the tube. The dissociation of O_2 is strongest in the tube and the O is blown out. The dissociation in the effluent is limited. In case of the plate electrode the plasma is more intense outside the tube, because the electric field is pulled out of the tube towards the plate (axial field). So the O production is more likely stronger outside the tube, resulting in a maximum O-density between the plate and the tube.

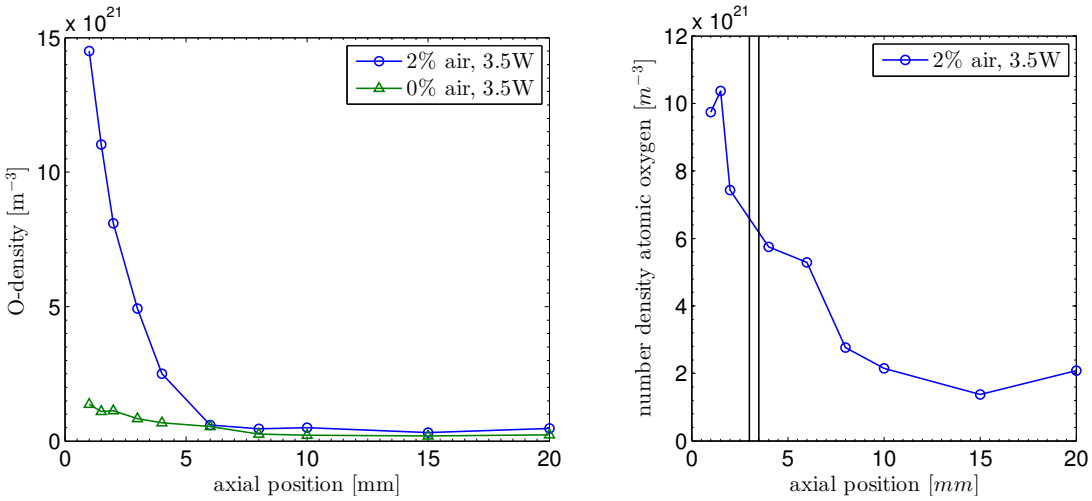

Figure 4.23: Axial profile of the atomic oxygen density in a rf-plasma jet with left the ring electrode and right the plate electrode. Measurements where performed with an argon flow of 1slm with 2% and 0% air. The vertical lines in the right figure indicate the position of the plate electrode, which completely blocked the measurement at 3mm.

The results presented in figure 4.23 for the measurements on a plasma with 3.5W plasma power and 0% added air concentration show that there is a signal up to 8 mm above the glass tube. There was no air added to the argon flow, but since a TALIF signal was measured, there has to be atomic oxygen present. This indicates that there is an influence of the surrounding air on the plasma. This could be expected because of the low gas flow and small tube diameter, which makes it easier for air to entrain. The calculation of the effective branching ratio a_O, for the calibration of the O density, is dependent on the added air concentration. The densities presented in figure 4.23 for 0% added air where calculated with an air concentration of zero percent, this can be interpreted as a quenching less TALIF process, which is incorrect. Because the amount of influence of ambient air on the plasma is not known, the atomic oxygen densities for the ring electrode configuration are calibrated for different air concentrations. The results are presented in figure 4.24. From this figure a maximum error at 1mm axial position of 40% for the 0% added air measurements can be found and a maximum error at 1mm axial position of 25% for the 2% added air measurements, assuming a deviation of 1% in the air concentration due to ambient air. More information is needed on the amount of entrainment of ambient air into the plasma to determine if the resulting error is negligible.

In the following measurement results the influence of ambient air has not been taken into account.

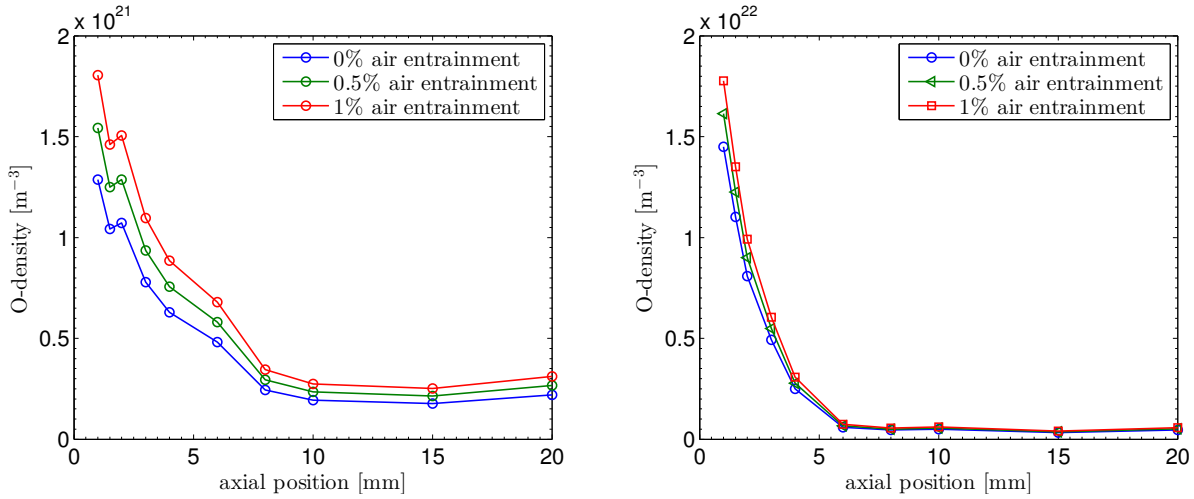

Figure 4.24: Axial profile of the number density of atomic oxygen when the influence of ambient air is taken into account. The concentrations in the legends of the graphs indicate the increase in air concentration, which is used to calculate the effective branching ratio. Left: A 3.5W rf-jet with ring electrode and a gas flow of 1slm argon + 0% air was used. Right: A 3.5W rf-jet with ring electrode and a gas flow of 1slm + 2% air was used.

4.2.4 plasma profile

By moving the rf-jet both in radial and axial direction, a plasma profile of the O density as presented in figure 4.25 can be obtained. The profile consists of 49 measurement points, seven in radial direction at 0, ±0.5, ±1.0, and ±1.5mm, and seven in axial direction at 1.0, 1.5, 2.0, 3.0, 4.0, 6.0, and 8.0mm.

The 2D plasma profile shows, like the axial profiles, that the O production is focused in the center of the plasma close by the glass tube and needle electrode.

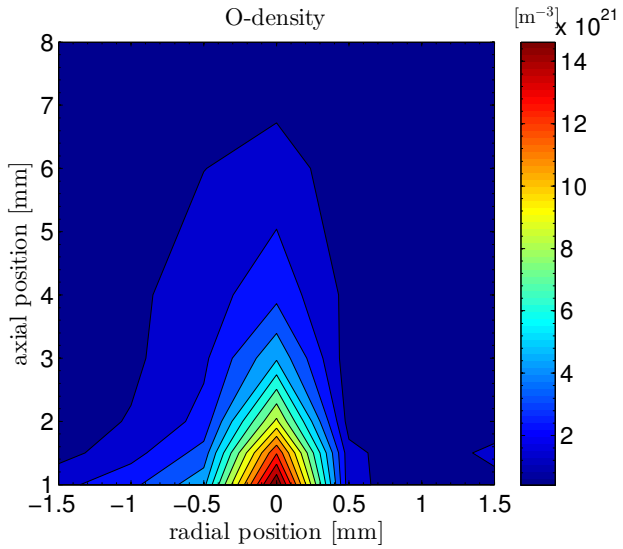

Figure 4.25: 2D profile of the number density of atomic oxygen in a 3.5W plasma with a flow of 1slm argon + 2% air. RF-jet with ring electrode configuration was used.

4.2.5 Concentration dependence

Figure 4.26 presents the atomic oxygen density for different gas mixtures, taken at 1mm axial position. The measurements where performed with the ring electrode configuration. For all species and concentrations the plasma power was adjusted to 3.5W.

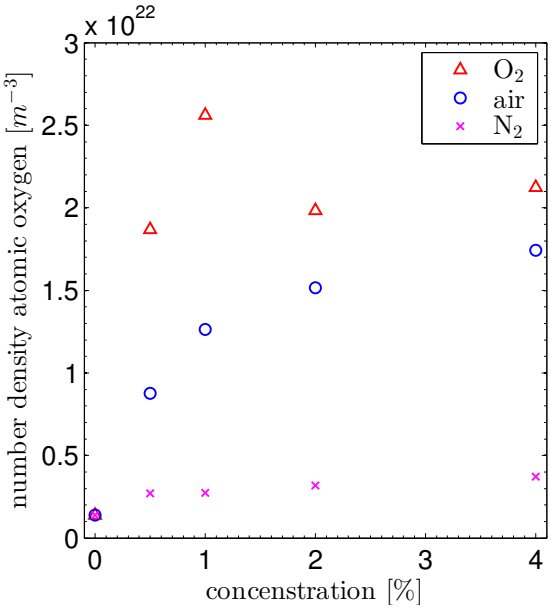

Figure 4.26: Number density of atomic oxygen in a 3.5W plasma of 1slm argon with different concentrations of admixtures measured at an axial position of 1mm. A rf-jet with ring electrode was used.

The air admixture causes an increase of the O production, but seems to saturate when the concentration is increased beyond 4%.

Adding O_2 to the argon flow causes a large increase in the O density until 1%, however for higher concentrations the O density decreases. This can be explained by the decrease in plasma size. When the concentration of the added species is increased, the plasma size becomes smaller, for equal plasma powers. The adding of O_2 to the admixture results in a smaller size plasma, than when an equal concentration of air or N_2 is added, so resulting in a steeper decrease due to shrinking of the plasma. However a maximum in the O-density as function of the added O_2 is also observed by [21], who measured the O and O_3 concentrations with mass spectrometry. Besides the decrease in O density, an increase in O_3 was observed. A possible explanation for this is that the O production from O_2 dissipation, which is limited by the electron density, is being competed with by reaction 2.3.2 consuming oxygen and producing ozone. The O_3 production, and therefore the O consumption, becomes more effective at higher O_2 ratios, thus the O_3 density increases and the O density decreases.

Adding N_2 to pure argon gives a small increase in O density. Because the oxygen can only come from the inflow of ambient air, the increase in O density is most likely an increase in O production through a chemical reaction between N_2 and air particles or products of air particles, as described by reactions 2.3.5, 2.3.6 and 2.3.7;

$$N + O_2 \rightarrow NO + O$$
$$N + NO \rightarrow N_2 + O$$
$$N_2 + O_2 \rightarrow N_2O + O.$$

4.2.6 Powers dependence

The O density for different plasma powers, taken at 1mm axial position, is shown in figure 4.27. The maximum plasma power that can be obtained depends i.a. on the electrode configuration and the positioning of the glass tube, in longitudinal direction. However plasma powers of 25W are very unlikely for the rf-jet. After the measurements, it was observed that the cover of the RF feed was partially melted and this can account for the high powers which are not absorbed in the plasma but mainly in a short cut introduced when the RF cable touched ground.

The density for the plate electrode configuration increases until a maximum density, it can be that the chemical reactions producing O and consuming O are in equilibrium, but, as described in section 2.3, this would mean that for a further increase in plasma power the O density would decrease.

For the ring electrode configuration the O density decreases when the plasma power exceeds 6.5W. The chemical shift in production and consumption of O, as described for the plate electrode, could be the cause, but because the setup was already damaged it is more likely that decrease in O is caused by the fact that the power measured does not correspond to the plasma power. This effect will mainly be an issue with larger RF voltages and thus higher powers.

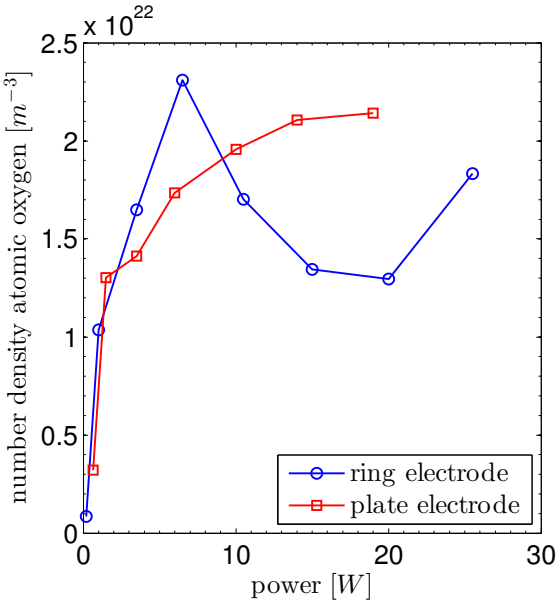

Figure 4.27: Number density of atomic oxygen in a plasma with a flow of 1slm argon + 2% air for different plasma powers.

4.2.7 Conclusion rf-measurements

The O density in case of the ring configuration is the highest close to the pin electrode. For the plate electrode the maximum density is found further above the nozzle, as a consequence of the difference in electric field lines.

There are uncertainties in the absolute calibration of the O-density for the rf-jet mainly because the air concentration added to the plasma is uncertain because of ambient air entrainment. With the addition of 2% air, O densities exceeding $10^{22}\mathrm{m}^{-3}$ are found. Similar dependences of power and air concentration are found as for the MW jet.

The measurements on the rf-jet do give a relative good idea of the effect on the O-density profile, when the added gas mixture or plasma power is changed. Although the larger powers need to be re-investigated to establish if an increase in power leads to a saturation of the O density or a decrease in the case of the ring electrode.

Chapter 5

General conclusion

Successful TALIF measurements in open environment were performed on both atomic oxygen in an atmospheric pressure plasma, as well as on xenon gas mixtures, making it possible to analyze the atomic oxygen in atmospheric pressure plasmas.

A calibration method with xenon gas was developed which can be applied at atmospheric pressure. This however requires a low pressure TALIF measurement to calibrate the quenching rate at atmospheric pressure. Ones the quenching rate at atmospheric pressure has been calibrated for a gas composition, (as is performed in this work) no more low pressure measurements are needed, provided that the TALIF measurement by atmospheric conditions is performed with the same gas composition. It is shown that the calibration method can also be applied on transitions, which occur as a result of collisional transfer.

For the microwave jet densities of $3.1{\cdot}10^{22}\mathrm{m}^{-3}$ and dissociation degrees of 50% were found in the core of the plasma close to the pin electrode, for a 30W plasma and a gas flow of 6slm helium + 3.2% air. The reproducibility of the measurement is within 20% accuracy, however the accuracy of the calibrated density is 60% as a result of the errors in the many parameters that were used for the calibration. The strong gas flow applied to the microwave jet makes the entrainment of ambient air into the plasma irrelevant.

Uncertain concentrations of ambient air entrainment made absolute calibration of the atomic oxygen density in the rf-plasmas impossible. O densities in the RF jet can be obtained which are similar compared to the MW jet. A possible underestimation of the air concentration would lead to even larger O densities.

The atomic oxygen density in the microwave plasma and the rf-plasma for the ring electrode configuration is highest close to the pin electrode, where the electron density is the highest. Suggesting that the dissociation of O_2 by free electrons or short lived or metastable species (such as N2(A,B)) has an important contribution to the production of atomic oxygen in atmospheric pressure plasmas.

Appendix A

List of experimental equipment

Talif set-up

Equipment	Type	Model
Amplifier	ORTEC	9306
Dye laser	Sirah Laser- und plasmatechnik GmbH	CSTR-LG-3000-HRR
Laser energy meter	OPHIR	PD10-V2-ROHS
Microwave power generator	Microtron 200	Mark 3
Monochromator	Jarrel Ash	
PCI board	FAST ComTec	P7888-2(E)
Photo multiplier tube (PMT)	Hamamatsu Photonics	R666S
Pump laser	Edgewave	IS6III-E YAG
Standards etc.	Thorlabs	
Flow controllers[1] (ranges 20 $sccm\ O_2$; 2 $slm\ He$; 10 $slm\ He$)	Brooks Instrument	5850E
Flow controller[1] (range 10 $sccm\ Ar$)	Brooks Instrument	5850TR

Vacuum set-up

Equipment	Brand	Model
Control valve	Pfeiffer	EVR 116
Pressure control unit	Pfeiffer	RVC 300
Pressure gauge (range 1000 $mbar$)	Pfeiffer	CMR271
Pressure gauge (range 11 $mbar$)	Pfeiffer	CMR363

Bibliography

[1] S Reuter, J Winter, A Schmidt-Bleker, D Schroeder, H Lange, N Knake, V Schulz-von Der Gathen, and K-D Weltmann. Atomic oxygen in a cold argon plasma jet: TALIF spectroscopy in ambient air with modelling and measurements of ambient species diffusion. *Plasma Sources Science and Technology*, 21(2):024005, 2012.

[2] AV Pipa, T Bindemann, E Kindel, J Ropcke, D Uhrlandt, and K Weltmann. Absolute measurement of Nitric Oxide production rate in atmospheric pressure plasma jet. *New Journal of Physics*, (12):724–727, 2007.

[3] N Knake, D Schröder, J Winter, and V Schulz-von Der Gathen. Investigations on the generation of atomic oxygen inside a capacitively coupled atmospheric pressure plasma jet. *Journal of Physics: Conference Series*, 227:012020, May 2010.

[4] A. F. H. Gessel, J. J. A. M. van der Mullen, and P. J. Bruggeman. Temperature and NO density measurements by LIF and OES in an atmaospheric pressure plasma jet. *Journal of Physics D: Applied Physics*, 46(9), 2013.

[5] AV Pipa, S Reuter, R Foest, and K-D Weltmann. Controlling the NO production of an atmospheric pressure plasma jet. *Journal of Physics D; Applied Physics*, 45(8):724–727, 2012.

[6] J Benedikt, D Hecimovic, D Ellerweg, and A von Keudell. Quadrupole mass spectrometry of reactive plasmas. *Journal of Physics D; Applied Physics*, 45, 2012.

[7] A. F. H. Gessel, K. M. J. Alards, and P. J. Bruggeman. NO production in an atmospheric pressure low temperature RF plasma jet. 2013.

[8] K Niemi, V Schulz-von der Gathen, and H F Döbele. Absolute atomic oxygen density measurements by two-photon absorption laser-induced fluorescence spectroscopy in an RF-excited atmospheric pressure plasma jet. *Plasma Sources Science and Technology*, 14(2):375, 2005.

[9] C. Tendero, C. Tixier, P. Tristant, J. Desmainson, and P. Leprince. Atmospheric pressure plasmas: A review. *Elsevier*, 2005.

[10] B Eliasson and U Kogelschatz. Modeling and applications of silent discharge plasmas. *IEEE Transactions on Plasma Science*, 19(2):309–323, 1991.

[11] G D Stancu, F Kaddouri, D a Lacoste, and C O Laux. Atmospheric pressure plasma diagnostics by OES, CRDS and TALIF. *Journal of Physics D: Applied Physics*, 43(12):124002, March 2010.

[12] G Dilecce, M Vigliotti, and S De Benedictis. A TALIF calibration method for quantitative oxygen atom density measurement in plasma jets. *Journal of Physics D: Applied Physics*, 33:53–56, 2000.

[13] NIST US Department of Commerce. NIST Atomic Spectra Database.

[14] K Niemi, V Schulz-von der Gathen, and H F Döbele. Absolute calibration of atomic density measurements by laser-induced fluorescence spectroscopy with two-photon excitation. *Journal of Physics D: Applied Physics*, 34:2330, 2001.

[15] Eric Weisstein Wolfram Research. MathWorld Convolution.

[16] B. Hrycak, M. Jasinski, and J. Mizeraczyk. Spectroscopic investigations of microwave microplasmas in various gases at atmospheric pressure. *The European Physical Journal D.*, 60:609–619, 2010.

[17] S Hofmann, A F H Van Gessel, T Verreycken, and P Bruggeman. Power dissipation, gas temperatures and electron densities of cold atmospheric pressure helium and argon RF plasma jets. *Plasma Sources Science and Technology*, 20(6):065010, 2011.

[18] R Saxon and J Eichler. Theoretical calculation of two-photon absorption cross sections in atomic oxygen. *Physical Review A*, 34(1):199–206, July 1986.

[19] M Uddi, N Jiang, E Mintusov, I V Adamovich, and W R Lempert. Atomic oxygen measurements in air and air/fuel nanosecond pulse discharges by two photon laser induced fluorescence. *Proceedings of the Combustion Institute*, 32(1):929–936, 2009.

[20] V Alekseev and D W Setser. Quenching Rate Constants and Product Assignments for Reactions of Xe(7p[3/2] 2 , 7p[5/2] 2 , and 6p[3/2] 2) Atoms with Rare Gases, CO, H 2 , N 2 O, CH 4 , and Halogen-Containing Molecules. *The Journal of Physical Chemistry*, 100(14):5766–5780, January 1996.

[21] D Ellerweg, J Benedikt, A von Keudell, N Knake, and V Schulz-von der Gathen. Characterization of the effluent of a He/O_2 microscale atmospheric pressure plasma jet by quantitative molecular beam mass spectrometry. *New Journal of Physics*, (12), 2010.